



biblio.ugent.be

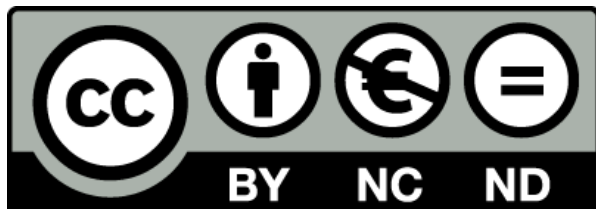
The UGent Institutional Repository is the electronic archiving and dissemination platform for all UGent research publications. Ghent University has implemented a mandate stipulating that all academic publications of UGent researchers should be deposited and archived in this repository. Except for items where current copyright restrictions apply, these papers are available in Open Access.

This is the Author Accepted Manuscript of the following article:

*Violette Deleeuw, Eric Carlson, Marjolijn Renard, Keith D Zientek, Phillip A Wilmarth, Ashok P Reddy, Elise C Manalo, Sara F Tufa, Douglas R Keene, Margie Olbinado, Marco Stampanoni, Sachiko Kanki, Hiromi Yanagisawa, Laura Muiño Mosquera, Patrick Sips, Julie De Backer, Lynn Y Sakai. "Unraveling the role of TGFβ signaling in thoracic aortic aneurysm and dissection using Fbn1 mutant mouse models." *Matrix Biol.* 2023:123:17-33.*

The final formal publication can be found at: <https://doi.org/10.1016/j.matbio.2023.09.001>

© 2023. This work is licensed under the Creative Commons [Attribution-NonCommercial-NoDerivatives 4.0 International](https://creativecommons.org/licenses/by-nc-nd/4.0/) license.



HIGHLIGHTS

- Reducing the expression of *Tgfb2* or replacing wildtype *Fbn1* with a mutant allele in which the first hybrid domain is deleted showed comparable deleterious effects on aortic disease severity in *Fbn1* mutant mice modeling Marfan syndrome.
- Reduced TGF β signaling and increased amounts of mast cell proteases were associated with aortic “microdissections” in mice in which the first hybrid domain is deleted in fibrillin-1.
- Increased quantities of extracellular matrix proteins were identified in *Fbn1* mutant mice with aortic aneurysm (without rupture).
- Marked reductions in quantities of fibrillins and microfibril proteins were revealed in *Fbn1* mutant mice with aortic aneurysm and rupture.
- Context-dependent effects on TGF β signaling were associated with *Fbn1* mutant mice representing mild to severe thoracic aortic disease.

1 **Unraveling the Role of TGF β Signaling in Thoracic Aortic Aneurysm and**
2 **Dissection Using *Fbn1* Mutant Mouse Models**

3
4 Violette Deleeuw^{a,1}, Eric Carlson^{b,1}, Marjolijn Renard^{a,c,1}, Keith D. Zientek^d, Phillip A.
5 Wilmarth^d, Ashok P. Reddy^d, Elise C. Manalo^c, Sara F. Tufa^c, Douglas R. Keene^c,
6 Margie Olbinado^e, Marco Stampanoni^e, Sachiko Kanki^f, Hiromi Yanagisawa^g,
7 Laura Muiño Mosquera^h, Patrick Sips^a, Julie De Backer^{i,2}, and Lynn Y. Sakai^{b,2}

8
9 ^a Department of Biomolecular Medicine, Ghent University, Corneel Heymanslaan 10, B-
10 9000 Ghent, Belgium

11 ^b Department of Molecular & Medical Genetics, Oregon Health & Science University,
12 3181 SW Sam Jackson Park Road, Portland, OR 97239

13 ^c Shriners Children's Hospital, 3101 SW Sam Jackson Park Road, Portland, OR 97239

14 ^d Proteomics Shared Resource, Oregon Health & Science University, 3181 SW Sam
15 Jackson Park Road, OR 97239

16 ^e Paul Scherrer Institute, Forschungsstrasse 111, 5232 Villigen, Switzerland

17 ^f Department of Thoracic and Cardiovascular Surgery, Osaka Medical and
18 Pharmaceutical University, 2-7 Daigaku-machi, Takatsuki, Osaka 569-0801 Japan

19 ^g Life Science Center for Survival Dynamics, Tsukuba Advanced Research Alliance,
20 The University of Tsukuba, Tsukuba, Ibaraki, 305-8577 Japan

21 ^h Department of Pediatrics, Division of Pediatric Cardiology, Ghent University Hospital,
22 Corneel Heymanslaan 10, B-9000 Ghent, Belgium

23 ¹ Department of Cardiology, Ghent University Hospital, Corneel Heymanslaan 10, B-
24 9000, Ghent, Belgium

25

26 ¹ Violette Deleeuw, Eric Carlson, and Marjolijn Renard contributed equally to this work.

27 ² Julie De Backer and Lynn Y. Sakai contributed equally as senior authors.

28

29

30 Corresponding Author:

31 Lynn Y. Sakai, Ph.D.

32 Department of Molecular & Medical Genetics

33 Oregon Health & Science University

34 Portland, OR 97239

35 shlys@ohsu.edu

36 ORCID: 0000-0003-0054-1539

37

38 **ABSTRACT**

39 Although abnormal TGF β signaling is observed in several heritable forms of thoracic
40 aortic aneurysms and dissections including Marfan syndrome, its precise role in aortic
41 disease progression is still disputed. Using a mouse genetic approach and quantitative
42 isobaric labeling proteomics, we sought to elucidate the role of TGF β signaling in three
43 *Fbn1* mutant mouse models representing a range of aortic disease from microdissection
44 (without aneurysm) to aneurysm (without rupture) to aneurysm and rupture. Results
45 indicated that reduced TGF β signaling and increased mast cell proteases were
46 associated with microdissection. In contrast, increased abundance of extracellular matrix
47 proteins, which could be reporters for positive TGF β signaling, were associated with
48 aneurysm. Marked reductions in collagens and fibrillins, and increased TGF β signaling,
49 were associated with aortic rupture. Our data indicate that TGF β signaling performs
50 context-dependent roles in the pathogenesis of thoracic aortic disease.

51

52 **KEYWORDS**

53 Fibrillin, Marfan syndrome, aortic aneurysm and dissection, TGF β signaling,
54 mouse models

55

56 INTRODUCTION

57 Marfan syndrome (MFS, OMIM #154700, ORPHA#558) is an autosomal dominant
58 pleiotropic connective tissue disorder with an estimated prevalence of 2 - 3 per 10,000
59 individuals. The main clinical manifestations of MFS are skeletal overgrowth, pectus
60 deformities, scoliosis, lens dislocation, thoracic aortic aneurysm and dissection/rupture
61 predominantly at the level of the sinuses of Valsalva, and mitral valve prolapse [1,2]. MFS
62 is caused by pathogenic variants in the gene encoding the extracellular matrix (ECM)
63 protein fibrillin-1 (*FBN1*) [3,4].

64 Initially, it was assumed that MFS features were caused by an inherent structural
65 weakness of tissues containing abnormal fibrillin-1 protein, which might hamper both
66 normal microfibril and elastic fiber assembly [5]. While this assumption still holds true,
67 the discovery that fibrillin-1 interacts directly with latent TGF β binding proteins (LTBPs)
68 raised the possibility that fibrillin-1 may also regulate TGF β bioavailability [6]. Findings in
69 lung tissue of *Fbn1^{mg Δ /mg Δ}* (*mg Δ /mg Δ*) mice indicated that fibrillin-1 deficiency resulted in
70 activation of TGF β signaling [7]. This interpretation was supported by rescue of the
71 abnormal lung phenotype in the mutant mice by administration of TGF β neutralizing
72 antibodies [7].

73 A causal relationship between fibrillin-1 variants and increased TGF β signaling
74 was extended to mitral valve prolapse, aortic aneurysm and muscle hypoplasia in another
75 MFS mouse model (*Fbn1^{C1039G/+}*, C1039G/+) [8-10]. *In vivo* administration of TGF β
76 neutralizing antibodies in C1039G/+ mice prevented aortic aneurysm development with
77 normalization of aortic root growth rate and aortic wall architecture [9]. Moreover,
78 losartan, an angiotensin II type 1 receptor (AT1R) antagonist (angiotensin receptor

79 blocker – ARB) with presumed TGF β neutralizing potential, prevented elastic fiber
80 fragmentation, reduced one TGF β signaling readout (positive pSmad
81 immunohistochemistry), and reduced aortic root growth [9]. These observations implied
82 that MFS-related aortic disease is driven by AT1R-dependent stimulation of the canonical
83 and non-canonical TGF β signaling pathways [9]. Subsequent large-scale clinical trials
84 with ARBs, either compared to, or in combination with, beta-blockers, unfortunately failed
85 to reproduce the same beneficial effects in humans [11-13].

86 The proposal that TGF β signaling is the main driver of pathogenesis in MFS [14]
87 is controversial. TGF β signaling may vary during the dynamic transition from initial
88 development of aortic aneurysm to end-stage disease (dissection and rupture). Indeed,
89 early inhibition of TGF β signaling by either TGF β neutralizing antibodies in *Fbn1*^{mgR/mgR}
90 (mgR/mgR) mice [15] or by genetic ablation of *Tgfbr2* in smooth muscle cells of C1039G/+
91 mice [16] exacerbated aortic disease. These results suggest that early in the aortic
92 disease process in MFS, TGF β signaling may be protective, rather than a driver of
93 pathogenesis.

94 The exact role of fibrillin-1 in the regulation of TGF β signaling remains unknown.
95 It was first suggested that TGF β is activated due to fibrillin-1 deficiency below a critical
96 threshold, leading to loss of TGF β sequestration in the matrix [7]. However, loss of TGF β
97 sequestration could in theory result in reduced, rather than increased, TGF β signaling,
98 depending on whether matrix sequestration of latent TGF β is necessary for activation of
99 TGF β . In order to specifically test the effects of a loss of the interaction between LTBP
100 and fibrillin-1, we first identified the LTBP binding site to be within the first hybrid domain
101 in fibrillin-1 [17] and then generated a mouse model in which the first hybrid domain is

102 deleted. Microfibrils in both heterozygous *Fbn1*^{H1Δ/+} (H1Δ/+) and homozygous
103 *Fbn1*^{H1Δ/H1Δ} (H1Δ/H1Δ) mice were assembled and exhibited normal fibrillin microfibril
104 ultrastructure, indicating that deletion of the first hybrid domain did not result in
105 compromised or reduced amounts of microfibrils. Moreover, these mutant mice lived long
106 lives and bred normally. Initial histological analysis of the aortic root showed no evidence
107 of fragmentation of the elastic lamellae [18]. Based on these initial results, we concluded
108 that activation of TGFβ signaling in MFS is not due to loss of binding of LTBP1s to fibrillin-
109 1.

110 The significance of the LTBP-fibrillin interaction, however, still remains unclear. Is
111 this interaction required for the appropriate targeting and sequestration of large latent
112 TGFβ complexes to the extracellular matrix, or can other matrix interactions suffice? If
113 the LTBP-fibrillin interaction is required for TGFβ signaling, then H1Δ/+ or H1Δ/H1Δ mice
114 should be expected to demonstrate phenotypes associated with a loss of TGFβ signaling.
115 In mice, complete loss of function mutations of *Tgfb1* are mostly embryonic lethal, but
116 survivors die neonatally from excessive inflammation. In contrast, *Tgfb2* null mice die
117 before birth or perinatally from developmental defects, which include defects in the
118 ascending aorta and outflow tract [19]. However, phenotypes associated with reduced
119 TGFβ signaling, rather than complete loss-of-function phenotypes, are difficult to predict.
120 In the present study, we aimed to investigate the requirement of the LTBP-fibrillin-1
121 interaction for TGFβ signaling in aortic homeostasis, using a mouse genetic approach.

122 We crossed our previously well-characterized *Fbn1*^{GT-8/+} (GT-8/+) *Fbn1* mutant
123 mouse model showing progressive thoracic aortic aneurysm development similar to aortic
124 disease observed in MFS [18,20] with other mutant mouse lines to generate the following

125 genotypes: *Fbn1*^{GT-8/H1Δ} (GT-8/H1Δ), double heterozygous *Fbn1*^{GT-8/+;}*Tgfb1*^{+/-} (GT-
126 8/Tgfb1) and *Fbn1*^{GT-8/+;}*Tgfb2*^{+/-} (GT-8/Tgfb2). With these mice, we document an isoform-
127 specific effect of TGFβ signaling in MFS aortic disease. Furthermore, we provide
128 evidence that deletion of the first hybrid domain in fibrillin-1 results in “microdissections”—
129 very localized aortic wall lesions—in the ascending aorta of H1Δ/+ mutant mice and in
130 severe aortic disease in GT-8/H1Δ. We can now present a spectrum of *Fbn1* mutant
131 mouse models of aortic disease from mild microdissection (H1Δ/+) to moderate
132 aneurysm-without-rupture (GT-8/+) to severe aneurysm-with-rupture (GT-8/H1Δ). We
133 used these *Fbn1* mutant mouse models to gain further insight into TGFβ signaling along
134 this spectrum of aortic disease.

135 RESULTS

136 ***Aortic disease severity is comparable in double heterozygous GT-8/Tgfb2 and*** 137 ***compound heterozygous GT-8/H1Δ mice***

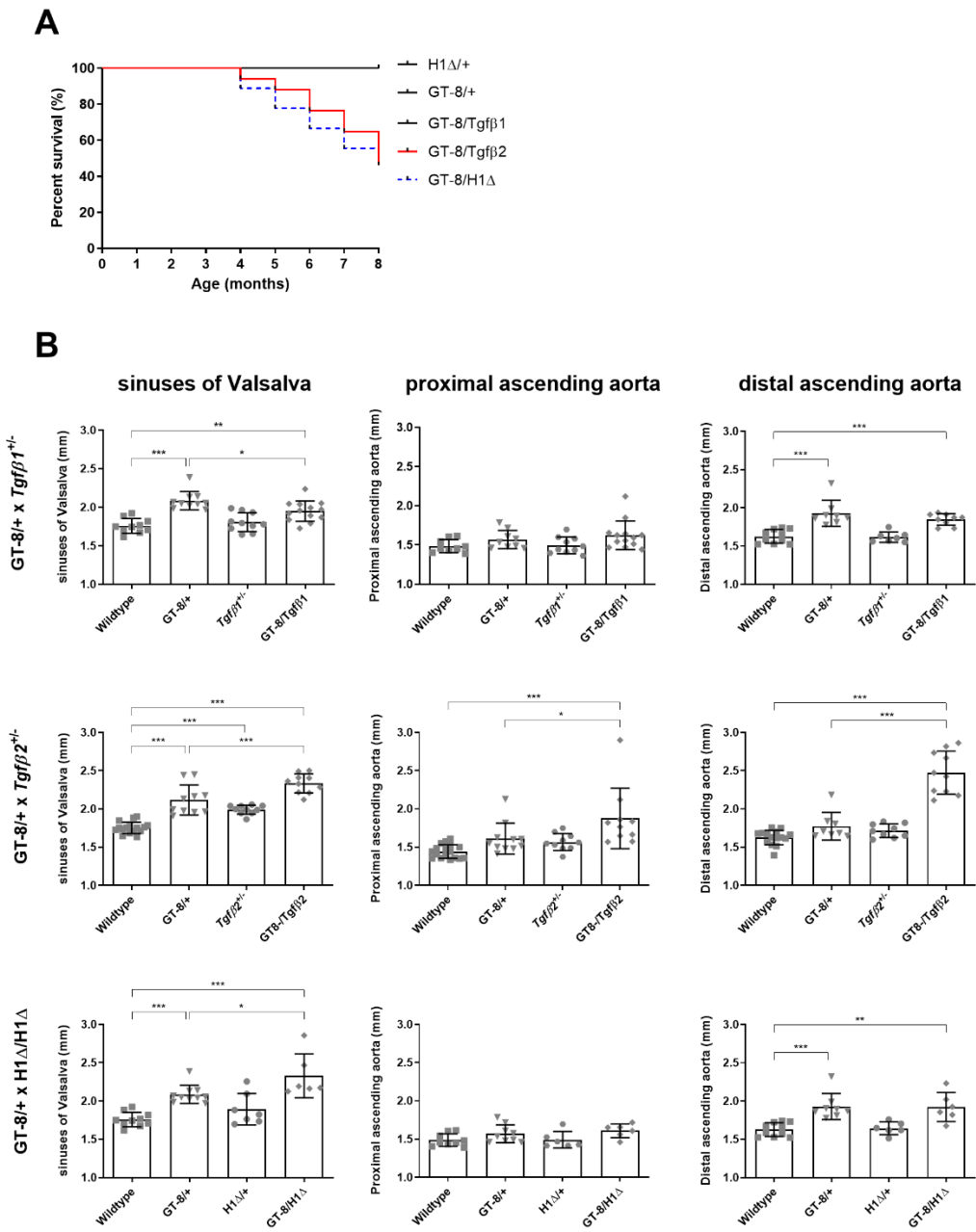
138 We assessed the effect of *Tgfb1* and *Tgfb2* haploinsufficiency, and the impact of
139 deleting the binding site in fibrillin-1 for large latent TGFβ complexes, in *Fbn1* mutant mice
140 presenting Marfan-like phenotypes (GT-8/+). Single mutant GT-8/+ and H1Δ/+ male
141 mice, as well as the double heterozygous GT-8/Tgfb1 mice had a normal life span. In
142 contrast, double heterozygous GT-8/Tgfb2 and compound heterozygous GT-8/H1Δ mice
143 suffered from sudden death with documented hemothorax, suggestive of aortic rupture
144 starting from the age of 4 months (Figure 1A). Eight of the 17 GT-8/Tgfb2 mice and four
145 of the nine GT-8/H1Δ mice died during the 8 months of study follow-up.

146 Aortic diameters in 6 months old male mice were measured using transthoracic
147 echocardiography (Figure 1B, Supplementary figure 1). GT-8/+, GT-8/Tgfb1, *Tgfb2*^{+/-},

148 GT-8/Tgf β 2 and GT-8/H1 Δ mice displayed significant enlargement of the aorta at the level
149 of the sinuses of Valsalva compared to wildtype mice (one-way ANOVA; **p < 0.01; ***p
150 < 0.001). However, double heterozygous GT-8/Tgf β 1 mice displayed significantly smaller
151 aortic root diameters compared to single mutant GT-8/+ mice (one-way ANOVA, *p <
152 0.05), while double heterozygous GT-8/Tgf β 2 mice and compound heterozygous GT-
153 8/H1 Δ mice showed significant enlargement of the aortic root compared to single mutant
154 GT-8/+ mice (one-way ANOVA; *p < 0.05; ***p < 0.01). Prominent differences in
155 ascending aortic size of double heterozygous GT-8/Tgf β 2 and compound heterozygous
156 GT-8/H1 Δ mice were observed when compared to single mutant *Tgf β 2^{+/-}* and GT-8/+
157 mice, and to wildtype (one-way ANOVA; *p < 0.05; **p < 0.01; ***p < 0.001). Aortic
158 dilatation of double heterozygous GT-8/Tgf β 2 mice was not restricted to the aortic root as
159 these mice also displayed significant increases in proximal and distal ascending aortic
160 diameters when compared to single mutant GT-8/+ mice (one-way ANOVA; *p < 0.05;
161 ***p < 0.01). In contrast, H1 Δ /+ and *Tgf β 1^{+/-}* mice had aortic diameters comparable to
162 wildtype mice. No differences in main pulmonary artery dimensions were observed
163 between the different genotypes and compared to wildtype (Supplementary figure 1).
164 Aortic valve regurgitation was observed in two GT-8/+ mice and one GT-8/H1 Δ mouse.
165 Mitral valve regurgitation was present in one GT-8/Tgf β 2 mouse. Finally, GT-8/Tgf β 2
166 mice also presented impaired diastolic function.

167 **Figure 1. Survival and aortic dimensions of the studied mouse models.** A) Survival
168 curve. Male GT-8/+, H1 Δ /+, and GT-8/Tgf β 1 mice (black line) had a normal life span. In
169 contrast, double heterozygous GT-8/Tgf β 2 (red line) and compound heterozygous GT-
170 8/H1 Δ mice (blue dashed line) died due to aortic rupture, starting from the age of 4

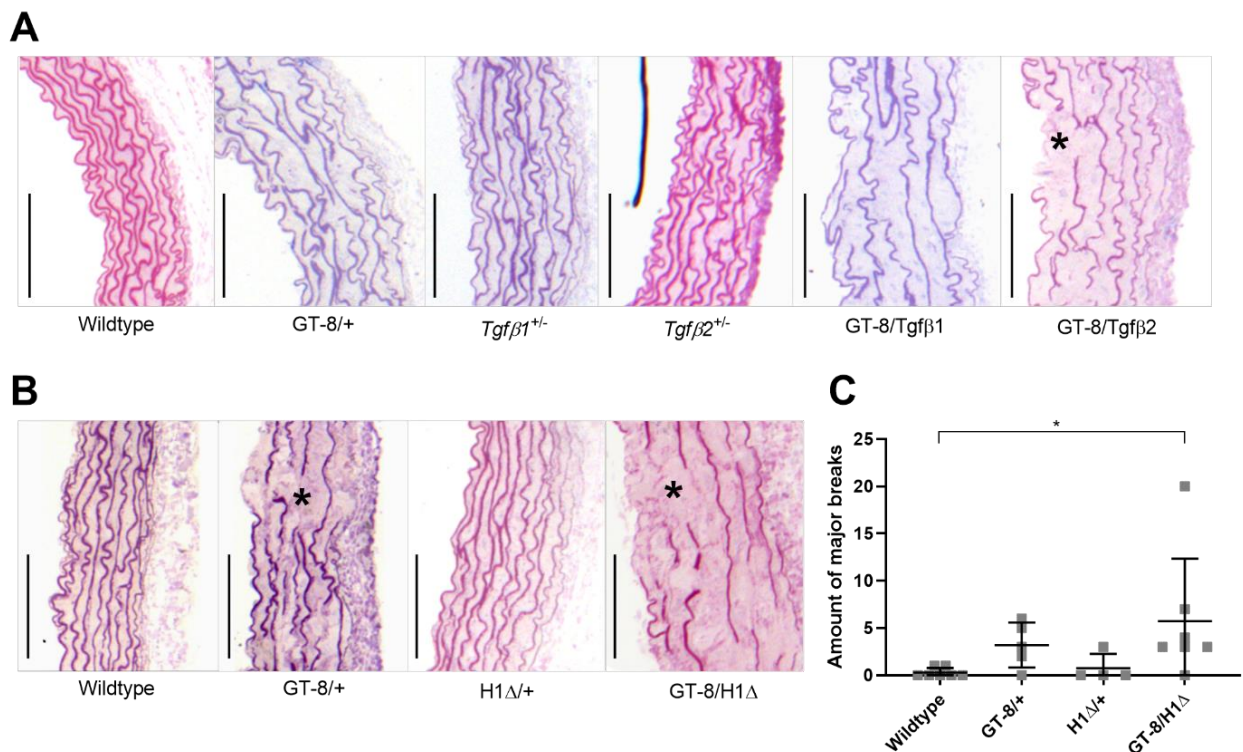
171 months. B) Cardiovascular ultrasound measurements of thoracic aortic segments in
 172 wildtype and *Fbn1* mutant mice. Aortic diameters at the sinuses of Valsalva, proximal
 173 ascending aorta, and distal ascending aorta in 6 months old male mice of the *Tgfb1*^{+/-}
 174 cross (top row), *Tgfb2*^{+/-} cross (middle row), and H1Δ/H1Δ cross (bottom row) are
 175 displayed. Results are presented as mean ± SD. *p < 0.05; **p < 0.01; ***p < 0.001



177 We next examined fragmentation of elastic lamellae in the aortic root (at the level
178 of the sinuses of Valsalva) of 6 month old wildtype and mutant GT-8/+, *Tgfβ2*^{+/-}, GT-
179 8/*Tgfβ1*, and GT-8/*Tgfβ2* mice (Figure 2A, Supplementary Figure 2) and in 8 month old
180 wildtype and mutant GT-8/+, H1Δ/+ and GT-8/H1Δ mice (Figure 2B, C) using histology.
181 As previously shown [20], aortic root dilatation in 8 month old GT-8/+ mice was associated
182 with increased fragmentation of the elastic lamellae, specifically the number of “major
183 breaks” (spanning at least three consecutive layers of elastic lamellae). Therefore, for
184 comparison, we examined aortic root histology in 8 month old GT-8/H1Δ mice. Because
185 double heterozygous mice for *Tgfβ2*^{+/-} and C1039G/+ demonstrated significant aortic
186 disease at the ages of 2 and 4 months [21], histology for the *Tgfβ1*^{+/-} and *Tgfβ2*^{+/-} crosses
187 with GT-8/+ was performed at a younger age. At 6 months of age, fragmentation of elastic
188 lamellae in GT-8/*Tgfβ2* aortic roots was significantly increased compared to age-matched
189 wildtype mice when single breaks were counted (Kruskal-Wallis test p= 0.0419; post hoc
190 Dunn’s test p=0.0345) (Supplementary Figure 2). More major breaks were observed in
191 the aortic roots from GT-8/*Tgfβ2* mice compared to age-matched wildtype and other
192 littermate genotypes (Figure 2A) but these results were not significant (Supplementary
193 Figure 2). At 8 months of age, major breaks were also increased in GT-8/H1Δ mice
194 compared to wildtype, GT-8/+, and H1Δ/+ mice (Kruskal-Wallis test p= 0.0165; post hoc
195 Dunn’s test p= 0.0168 was significant compared to wildtype) (Figure 2B, C). Major breaks
196 were mostly present on the luminal side of the medial layer. *Tgfβ1*^{+/-} and H1Δ/+ mice
197 displayed aortic root morphology similar to wildtype mice. However, one out of four H1Δ/+
198 mice also seemed to display multiple major breaks in the aortic root even though aortic
199 root dimensions were similar to those of wildtype mice.

201 **Figure 2. Aortic wall morphology in the aortic roots of *Fbn1* mutant mouse models.**

202 A) Representative histology of the aortic root of 6 month old male wildtype and GT-8/+
203 mice crossed with *Tgfb1*^{+/-} mice and with *Tgfb2*^{+/-} mice. Elastic fiber fragmentation was
204 observed in the aortic root of GT-8/+, *Tgfb2*^{+/-}, GT-8/*Tgfb1*, and GT-8/*Tgfb2* mice.
205 However, major breaks were observed only in roots from GT-8/*Tgfb1* and GT-8/*Tgfb2*
206 mice. B) Representative histology of the aortic root of 8 month old male wildtype, GT-
207 8/+, H1Δ/+, and GT-8/H1Δ mice. C) Overview of the number of major breaks in the
208 aortic root of 8 month old male wildtype and GT-8/+ mice from the cross with H1Δ/H1Δ.
209 GT-8/H1Δ mice had significantly more major breaks in the aortic root (Kruskal-Wallis test
210 p= 0.0165; post hoc Dunn's test p = 0.0168). Major breaks (fragmentation over ≥ 3 layers
211 of elastic lamellae) are indicated by an asterisk in panels A and B. Scale bars = 100 μm.
212 Results are presented as mean ± SD. *p < 0.05

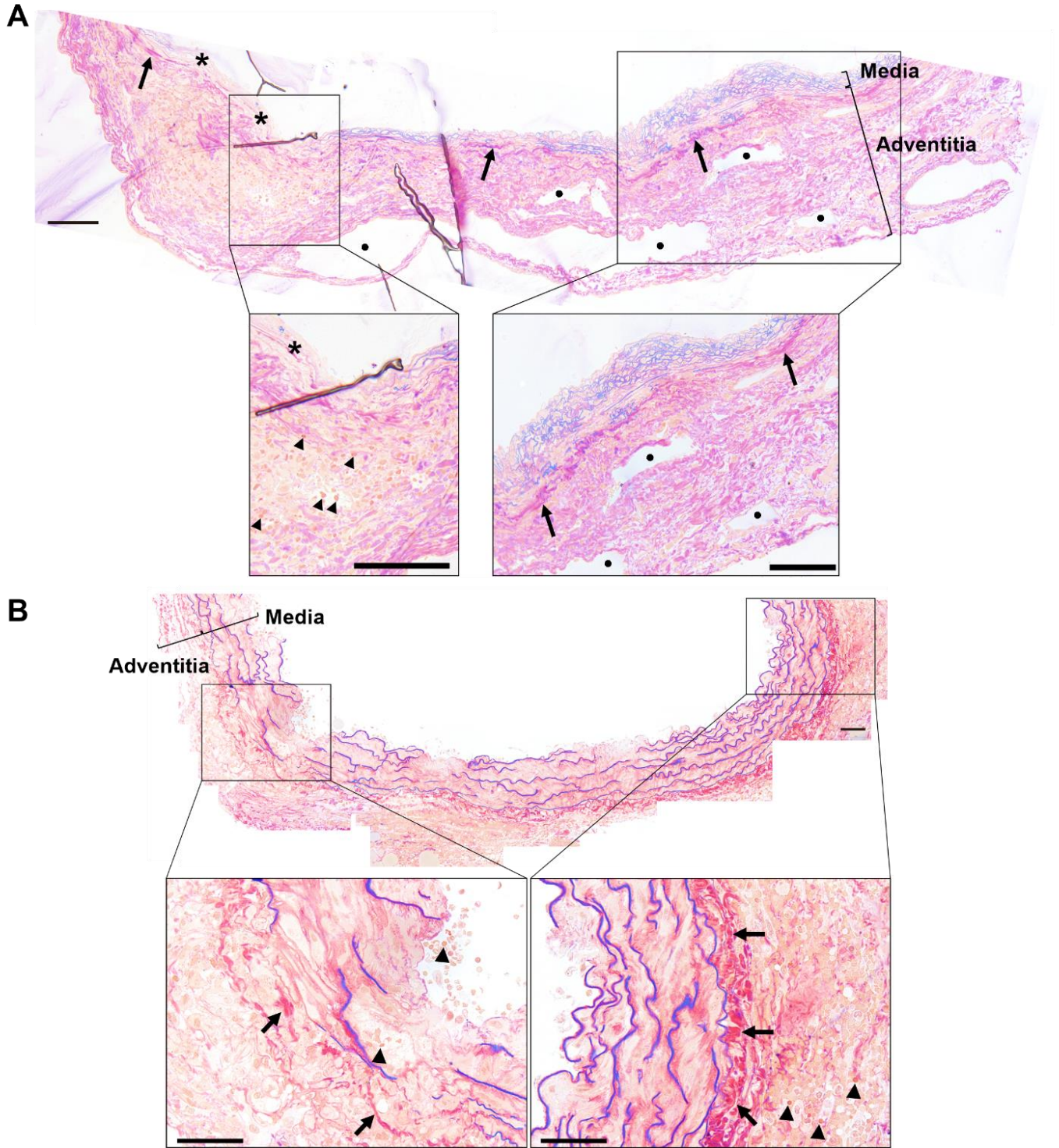


214 We also assessed aortic root pathology in *Fbn1* mutant mice at the end-stage of
215 aortic disease. Light microscopy showed extensive changes in the aortic wall of both
216 mutants—GT-8/H1 Δ and GT-8/Tgf β 2—destined to die early from aortic rupture (Figure
217 3). In addition to extensive elastic fiber fragmentation, regions of focal loss of elastic
218 lamellae were also observed in the tunica media along with substantial thinning of the
219 medial layer of the aorta. The tunica adventitia was expanded with the presence of thick
220 collagen bundles, infiltration of leucocytes and macrophages, and increased
221 vascularization. These end-stage histological findings were never observed in wildtype
222 or in GT-8/+ mice between 8 and 12 months of age [22].

223

224 **Figure 3. End-stage aortic wall morphology in the aortic roots of GT-8/H1 Δ and GT-**
225 **8/Tgf β 2 mice.** A) Representative aortic wall morphology of the aortic root of an 8 month
226 old male GT-8/H1 Δ mouse showing extensive fragmentation of the elastic lamellae, focal
227 loss of elastic lamellae (marked with asterisks), thinning of the medial layer of the aorta,
228 the presence of thick collagen bundles (indicated with black arrows) in the adventitia,
229 infiltration of leucocytes and macrophages (indicated with black arrowheads) and
230 increased vascularization of the adventitia (marked with black dots). Scale bars = 100
231 μ m. B) Aortic wall morphology of the aortic root of a 10 month old male GT-8/Tgf β 2
232 mouse, showing extensive elastic lamellae fragmentation, increased collagen deposition
233 (indicated with black arrows), and infiltration of inflammatory cells (indicated with black
234 arrowheads). Scale bars = 50 μ m. Aortic root tissues were stained using the polychrome
235 stain of Van Reempts and Borgers as follows: nuclei, dark brown; cytoplasm, yellow;

236 collagen fibrils, red; elastic fibers, blue; intracytoplasmic glycogen and mucus, blue and
237 violet, respectively; and other cytoplasmic inclusions, orange to red.

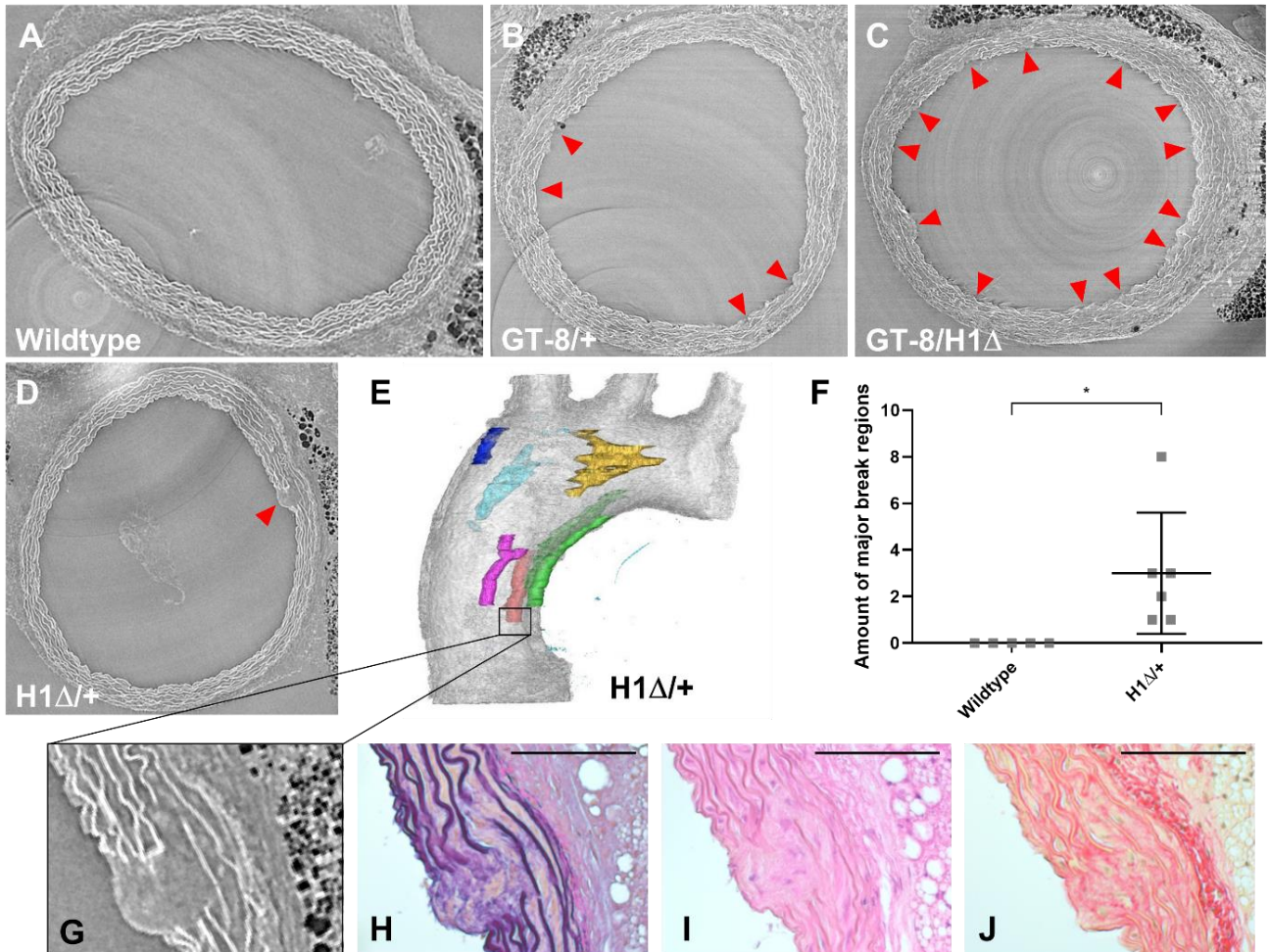


239 ***H1Δ/+ mice have microdissections in the ascending aortic wall***

240 Histology of aortic root sections revealed multiple major breaks in one of four eight
241 month old H1Δ/+ mice (Figure 2B, C). To further explore the effects of deleting the first
242 hybrid domain in fibrillin-1, we focused on aortic wall morphology of the entire ascending
243 aorta. *Ex vivo* synchrotron microCT imaging showed marked differences in elastic fiber
244 integrity between the ascending thoracic aorta of 6 month old male *Fbn1* mutant mice
245 compared to wildtype controls (Figure 4A – D, Supplementary Figure 3). Aortic aneurysm
246 in the ascending aorta of both GT-8/+ and GT-8/H1Δ mice (Figure 4B, C) was associated
247 with extensive fragmentation of the elastic lamellae and major breaks (indicated with red
248 arrowheads). In contrast, synchrotron imaging of the ascending thoracic aorta of H1Δ/+
249 mice, which showed no evidence of aneurysm (Figure 1B), revealed areas of
250 microdissection (indicated with red arrowhead), defined as focal lesions in the aortic wall
251 (Figure 4D). Compared to wildtype, 3D reconstructions of synchrotron-based microCT
252 imaging of the aortic wall of H1D/+ mice showed significantly increased areas of
253 microdissection in the ascending aorta (Figure 4E), ranging from a minimum of one to a
254 maximum of eight regions per aorta (Wilcoxon signed-rank test $p = 0.0372$) (Figure 4F).
255 Histological sections taken from these areas of microdissection confirmed the presence
256 of extensive fragmentation of the elastic lamellae and displayed cellular influx and
257 increased collagen deposition (Figure 4F – J). These areas of *very localized vascular*
258 *wall lesions* in the ascending thoracic aorta in H1Δ/+ were similar to those seen with
259 synchrotron imaging in the ascending thoracic aorta of 6 month old GT-8/+ and GT-8/H1Δ
260 mice, although the latter two models showed more extensive fragmentation and major
261 breaks in the elastic lamellae (Supplementary Figure 3). Synchrotron imaging of the

262 ascending thoracic aorta of wildtype mice showed no areas of major breaks in the elastic
263 lamellae (Figure 4A, F).

264 **Figure 4. Synchrotron imaging of the ascending thoracic aorta of *Fbn1* mutant**
265 **mice.** Synchrotron-based micro-CT imaging of the ascending thoracic aortic wall of 6
266 month old (A) wildtype, (B) GT-8/+, (C) GT-8/H1Δ, and (D) H1Δ/+ mice. E) 3D
267 reconstruction of synchrotron-based micro-CT scan of the aortic wall of a 6 month old
268 male H1Δ/+ mouse. Colored regions indicate sites where major breaks in the elastic
269 lamellae were observed. F) Overview of the number of regions of major breaks in the
270 ascending aorta of 6 month old male H1Δ/+ mice and wildtype controls (Wilcoxon signed-
271 rank test $p = 0.0372$). G) Section taken from the area marked with a black line in Figure
272 4E. A clear major break across four to five elastic lamellae can be seen in the magnified
273 image by H) Resorcin-Fuchsin elastin staining. I) Hematoxylin-Eosin (H&E) staining
274 displayed cellular influx. J) Picro-Sirius Red (PSR) staining indicated increased collagen
275 deposition. Scale bars = 100 μm . Results are presented as mean \pm SD. * $p < 0.05$



276

277 **Quantitative proteomics analyses suggest reduced TGFβ signaling in H1Δ/+**
 278 **ascending aorta**

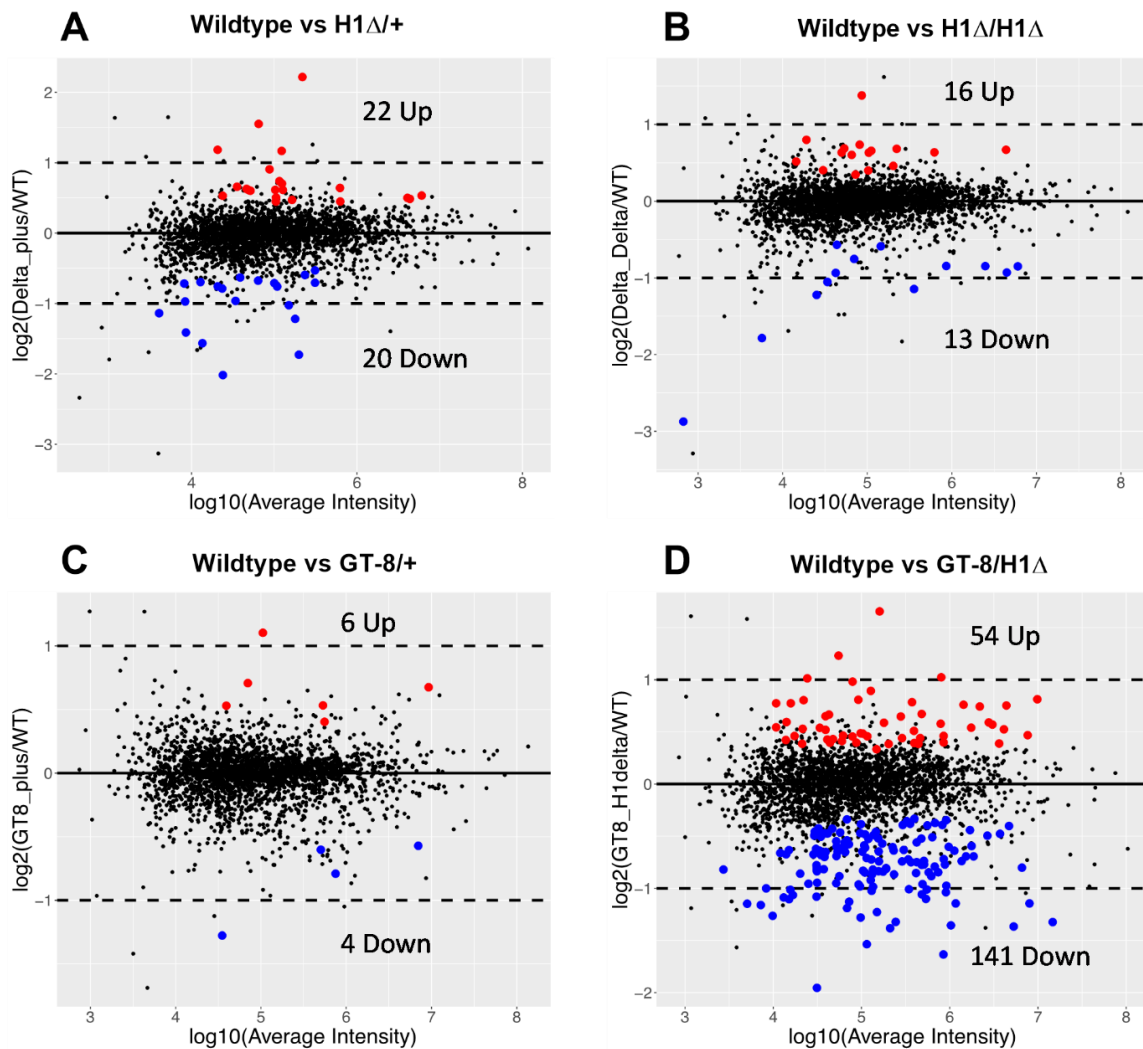
279 In order to delve more deeply into molecular mechanisms underlying aortic disease
 280 in the different *Fbn1* mutant mouse models, proteins present in the ascending aorta from
 281 4 month old male mice of each genotype were quantitated using tandem mass tag (TMT)
 282 isobaric-labeling and mass spectrometry. The ascending aorta of male mice was
 283 selected for analysis because both ultrasound (Figure 1B) and morphological data
 284 (Figures 2,4) showed significant evidence of disease in both the ascending aorta and the
 285 root. The age of 4 months was selected because GT-8/H1Δ mice begin to die from aortic

286 rupture at this time (Figure 1A). There were 285,288 instrument scans (peptide
287 sequencing attempts) acquired for the TMT plex with the male samples. The 48,311
288 scans with successful peptide sequence assignments (at a 1% scan FDR) mapped to
289 2,805 protein sequences after parsimonious protein grouping (excluding common
290 contaminants). We were able to quantify 2,721 of those proteins. The complete list of
291 identified proteins, reporter ion intensities, and statistical testing results are in
292 Supplementary Excel File 1.

293 Differential abundance MA plots of significantly increased or decreased proteins
294 (red or blue dots, respectively) are shown for each genotype compared to wildtype in
295 Figure 5A-D. Aortic dimensions in male GT-8/+ mice are significantly larger than wildtype
296 at the sinuses of Valsalva at 4 months of age, while the proximal and distal ascending
297 aorta are not significantly enlarged [20]. Therefore, it is not surprising that relatively few
298 significant differences in protein abundances (six increased; four reduced) were observed
299 at 4 months of age in the full ascending aorta of GT-8/+ mice compared to wildtype. There
300 were more differences identified between 4 month old H1Δ/+ and wildtype (22 increased;
301 20 reduced) and between H1Δ/H1Δ and wildtype (16 increased; 13 reduced), even
302 though aortic dimensions in 6 month old H1Δ/+ mice were similar to wildtype (Figure 1B).
303 However, the large numbers of significant differences in proteins identified in GT-8/H1Δ
304 mice compared to wildtype (54 increased; 141 reduced) were in concert with the severe
305 aortic phenotype observed in GT-8/H1Δ mice.

306 **Figure 5. Proteomic profiles of ascending aorta in *Fbn1* mutant mice.** A-D)
307 Representation of identified proteins in the ascending thoracic aorta of 4 month old male
308 wildtype, H1Δ/+, H1Δ/H1Δ, GT-8/+, and GT-8/H1Δ mice using TMT-labeling and mass

309 spectrometry. All 2,721 proteins are displayed in MA plots according to their log₂ fold-
310 change (y-axis) and their log₁₀ average intensity (total reporter ion intensity per protein,
311 x-axis) with significantly increased or decreased proteins highlighted in red and blue dots
312 respectively. Black dots represent identified proteins whose relative abundances were
313 not significantly different from wildtype.



314

315 Proteins associated with TGFβ signaling were selected for further analysis.
316 Selected proteins are shown in Table 1. The presence of LTBP-1 and LTBP-4 was
317 evident in H1Δ/+ and H1Δ/H1Δ aortic tissues, even though the binding site in fibrillin-1 for

318 these LTBP's was deleted in these mice. However, LTBP-1 and LTBP-4 were reduced in
319 these mice compared to wildtype. The abundance of TGF β 2 was also reduced in both
320 H1 Δ /+ and H1 Δ /H1 Δ aortic tissues, while TGF β R1 and SMAD2 were equivalent to
321 wildtype. Moreover, Col1a1, Col1a2, and Col3a1, classical extracellular matrix reporter
322 molecules for positive TGF β signaling, as well as plasminogen activator inhibitor (PAI-1),
323 another molecule highly induced by TGF β signaling, were all reduced in H1 Δ /+ and
324 H1 Δ /H1 Δ aortic tissues. While the Benjamini-Hochberg adjusted p-values (a false
325 discovery rate) were not significant for each individual protein difference, collectively
326 these differences in abundance suggest a reduction in TGF β signaling in H1 Δ /+ and
327 H1 Δ /H1 Δ aortic tissues.

328 In contrast to these values in H1 Δ /+ and H1 Δ /H1 Δ aortic tissues, LTBP-1 (but not
329 LTBP-4), TGF β 2, TGF β R1, SMAD2, and Col1a1, Col1a2, Col3a1, and PAI-1 were
330 increased in GT-8/+ aortic tissue, compared to wildtype. These data are consistent with
331 an increase in TGF β signaling, and previously described increases in collagen content in
332 aortic aneurysm. Again, the adjusted p-values for individual increases compared to
333 wildtype were not statistically significant, but taken together, these data suggest a trend
334 toward increased TGF β signaling in GT-8/+ aortic tissue.

335

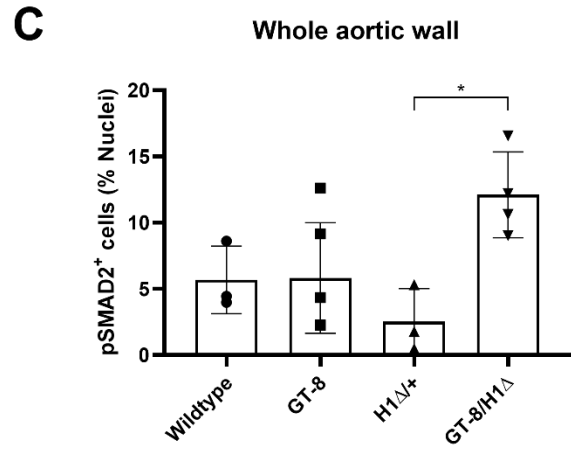
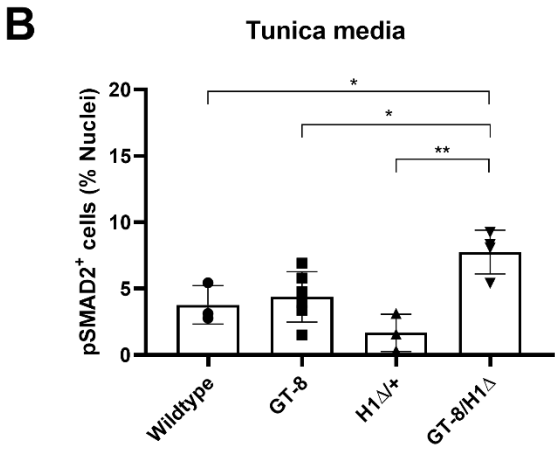
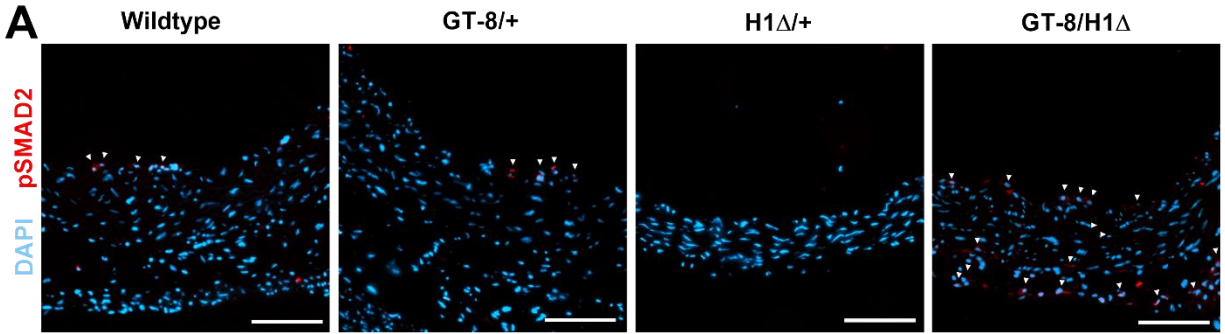
336 **Table 1. Relative abundances of proteins involved in the TGF β signaling pathway**
337 **in ascending thoracic aorta in *Fbn1* mutant mice.** Relative abundances of proteins
338 associated with the TGF β signaling pathway were obtained by isobaric-labeling
339 quantitative proteomics. Average total protein reporter ion intensities (measurements for
340 relative abundance) are displayed for each genotype, along with fold changes (% change)
341 compared to wildtype, and Benjamini-Hochberg adjusted p-values. The rank order of
342 abundance for each protein within our database of 2721 proteins is indicated in
343 parentheses under the protein name. The number analyzed for each genotype is listed
344 as n=2 or n=3. Standard deviations are listed in parentheses below the average reporter
345 ion intensities. Except for LTBP-4 in GT-8/H1 Δ , the adjusted p-values for each individual
346 protein are not significant. Note: The FDR significance cutoff is 0.1 (rather than 0.05).
347 Shading was assigned according to fold change: none = fold change $\leq \pm 1.1$, lightest
348 shade = fold change $\pm 1.1 - \leq 1.3$, medium shade = fold change $\pm 1.3 - \leq 1.5$, and darkest
349 shade = fold change > 1.5 . Orange shading represents increased fold changes; blue
350 shading, decreased fold changes.

351

Protein	Wildtype (n=3)	H1Δ/+ (n=2)	H1Δ/H1Δ (n=2)	GT-8/+ (n=3)	GT-8/H1Δ (n=2)
LTBP1 (190)	1,487,271 (246,919)	1,138,035 (145,487) -1.31 (-24%) p = 0.45	1,314,866 (210,590) -1.13 (-12%) p = 0.92	1,654,115 (436,815) 1.11 (11%) p = 0.99	1,144,128 (132,473) -1.3 (-23%) p = 0.40
LTBP3 (1105)	125,511 (19,002)	114,179 (8,221) -1.1 (-9%) p = 0.77	115,456 (17,676) -1.09 (-8%) p = 0.93	112,593 (19,713) -1.12 (-11%) p = 0.96	89,751 (2,107) -1.4 (-29%) p = 0.11
LTBP4 (153)	1,889,869 (163,561)	1,504,798 (219,134) -1.26 (-21%) p = 0.42	1,765,666 (349,029) -1.07 (-7%) p = 0.94	1,638,352 (293,498) -1.15 (-13%) p = 0.87	1,168,472 (42,422) -1.62 (-38%) p = 0.01
TGFβ2 Proprotein (2124)	21,690 (1,587)	19,198 (3,785) -1.13 (-12%) p = 0.71	18,419 (2,818) -1.18 (-15%) p = 0.88	23,567 (3,571) 1.09 (9%) p = 0.99	20,686 (2,898) -1.05 (-5%) p = 0.88
TGFβR1 (2375)	12,836 (926)	13,649 (429) 1.06 (6%) p = 0.85	13,721 (196) 1.07 (7%) p = 0.94	14,397 (2,793) 1.12 (12%) p = 0.94	15,294 (724) 1.19 (19%) p = 0.49
SMAD2 (2547)	5,175 (730)	5,550 (1,038) 1.07 (7%) p = 0.86	5,606 (474) 1.08 (8%) p = 0.94	5,804 (508) 1.12 (12%) p = 0.99	6,998 (664) 1.35 (35%) p = 0.26
PAI 1 (2094)	23,598 (3,014)	21,308 (1,780) -1.11 (-10%) p = 0.88	16,081 (6,620) -1.47 (-32%) p = 0.83	29,292 (11,569) 1.24 (24%) p = 0.93	28,711 (8,356) 1.22 (22%) p = 0.69
Col1a1 (1)	126,102,169 (30,660,521)	108,338,206 (25,763,985) -1.16 (-14%) p = 0.83	114,490,151 (3,451,286) -1.1 (-9%) p = 0.96	145,746,370 (51,252,792) 1.16 (16%) p = 0.99	82,007,269 (42,941,159) -1.54 (-35%) p = 0.39
Col1a2 (6)	55,228,155 (15,622,198)	45,112,359 (14,164,113) -1.22 (-18%) p = 0.81	48,664,616 (1,361,580) -1.14 (-12%) p = 0.95	62,409,384 (25,630,042) 1.13 (13%) p = 0.99	32,380,689 (18,182,339) -1.71 (-42%) p = 0.34
Col3a1 (7)	50,756,346 (14785676)	37,384,279 (146,910) -1.36 (-26%) p = 0.81	39,383,931 (5,915,312) -1.29 (-22%) p = 0.95	56,132,536 (23,938,375) 1.11 (11%) p = 0.99	25,699,419 (12,165,451) -1.98 (-49%) p = 0.34

354 To further assess the status of TGF β signaling, we used immunofluorescent
355 staining to examine the phosphorylation state of the previously established TGF β
356 signaling downstream effector SMAD2 in the ascending thoracic aorta (Figure 6). We
357 evaluated the nuclear localization of the phosphorylated form of SMAD2 (pSMAD2) in the
358 tunica media (Figure 6B) as well as in the whole aortic wall (Figure 6C). Levels of
359 pSMAD2 tended to be reduced in the tunica media and in the whole aortic wall of H1 Δ /+
360 mice compared to wildtype (one-way ANOVA $p < 0.05$; post hoc Sidak test $p = 0.0035$
361 and $p = 0.8153$, respectively). In contrast, pSMAD2 levels in the tunica media and whole
362 aortic wall of GT-8/+ mice were similar to those in wildtype (one-way ANOVA $p < 0.05$;
363 post hoc Sidak test $p = 0.9927$ and $p > 0.9999$, respectively). pSMAD2 levels were
364 increased in the tunica media of GT-8/H1 Δ mice (one-way ANOVA $p < 0.05$; post hoc
365 Sidak test $p < 0.05$ and $p = 0.1498$, in the tunica media and whole aortic wall respectively).

366 **Figure 6. Immunostaining for pSMAD2 in ascending thoracic aorta of *Fbn1* mutant**
367 **mice.** A) Representative images of ascending aortic tissues from 6 month old male
368 wildtype, GT-8/+, H1 Δ /+, and GT-8/H1 Δ mice. DAPI (blue) and pSMAD2 (red) staining
369 is displayed, nuclear localization of pSMAD2 is indicated by a white arrowhead. Scale
370 bars = 100 μ m. Percentage of pSMAD2-positively stained nuclei in the tunica media (B)
371 and entire wall thickness (C). $n = 3 - 6$ mice per group. Results are presented as mean \pm
372 SD. * $p < 0.05$; ** $p < 0.01$.



373

374

375 ***Extracellular matrix changes in the ascending thoracic aorta distinguish Fbn1***
 376 ***mutant mice with aneurysm from mice with aneurysm/rupture***

377

378

379

380

381

382

383

384

At 4 months of age, aortic disease in GT-8/H1 Δ mice is entering the end stage, and mice begin to die from aortic rupture (Figure 1A). At this time, in addition to marked reductions in LTBP3 and collagens (Table 1), other extracellular matrix proteins, especially microfibril proteins (Table 2), were also found to be reduced in GT-8/H1 Δ aortic tissue, dramatically foreshadowing the collapse of the aortic wall. These reductions occurred in spite of increased TGF β receptor and increased SMAD2 concentrations (Table 1) as well as increased SMAD2 phosphorylation in GT-8/H1 Δ aortic tissue (Figure 6) (one-way ANOVA $p < 0.05$; post hoc Sidak test $p < 0.05$ and $p = 0.1498$, in the tunica

385 media and whole aortic wall respectively). Of the eight matrix proteins that were
386 significantly reduced in GT-8/H1Δ aortic tissue, only two (versican and MFAP-4) were
387 significantly reduced in GT-8/+ aortic tissue (Table 2). Only one (fibronectin) of the seven
388 significantly increased matrix proteins in GT-8/H1Δ aortic tissue was also increased in
389 GT-8/+ aortic tissue (Table 2). Many of the extracellular matrix proteins listed as
390 increased in aortic tissues are known to be direct targets of TGFβ signaling [23].

391

392 **Table 2. Extracellular matrix proteins that are differentially quantified in *Fbn1***
393 **mutant thoracic ascending aortae relative to wildtype.** Extracellular matrix protein
394 abundances in the ascending thoracic aorta of 4 month old male mice of the two mutant
395 genotypes, compared to wildtype, were compared after TMT-labeling and mass
396 spectrometry. Fold change = A/B, where A is the mean TMT reporter ion intensity for GT-
397 8/H1Δ or GT-8/+, and B is wildtype. When A is less than B, fold changes are computed
398 as B/A and have negative signs. Common proteins that are significantly increased or
399 decreased in both genotypes, compared to wildtype, are highlighted in red.

Protein	Fold Change GT-8/H1Δ vs Wildtype	Adjusted p-value	Fold Change GT-8/+ vs Wildtype	Adjusted p-value
Tenascin	1.9	0.04	1.5	0.39
Fibronectin	1.8	0.0007	1.6	0.02
Col14a1	1.7	0.06	1.1	0.99
Slit-3	1.5	0.001	1.3	0.14
VWA1	1.4	0.02	1.3	0.26
Nidogen-1	1.4	0.15	1.3	0.28
Aggrecan	1.4	0.03	1.2	0.33
Glypican-4	1.4	0.01	1.2	0.29
Fibulin-2	1.4	0.25	1.5	0.21
Laminin α5	1.4	0.12	1.4	0.11
Integrin α5	1.3	0.1	1.3	0.21
Glypican-6	1.3	0.19	1.1	0.87
Integrin α3	1.3	0.12	1.2	0.32
SPARC	1.2	0.45	1.3	0.28
Elastin	-2.6	0.16	1.1	0.99
Fibrillin-1	-2.5	0.00007	-1.4	0.41
MFAP-2 (MAGP1)	-2	0.0009	-1.2	0.7
Fibrillin-2	-1.9	0.001	-1.1	0.99
Versican	-1.8	0.0007	-1.7	0.0006
MFAP-4	-1.7	0.0005	-1.5	0.02
Lrc17	-1.7	0.007	-1.5	0.11
Col6a6	-1.6	0.002	-1.3	0.24
LTBP-4	-1.6	0.01	-1.2	0.87
Hapln1	-1.4	0.13	-1.5	0.16
LTBP-3	-1.4	0.11	-1.1	0.96
CCN-5	-1.3	0.14	-1.2	0.76
ADAM-10	-1.3	0.16	1.0	0.99

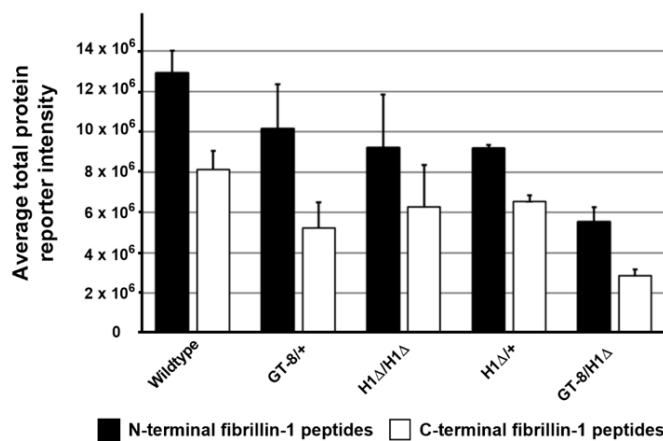
400

401 The abundance of fibrillin-1 was significantly reduced in GT-8/H1Δ aortic tissue
402 compared to wildtype (-2.5 fold, p = 0.00007). Further analysis of fibrillin-1 peptides
403 indicated that there were 109 distinct peptides, unique to fibrillin-1, spanning residues
404 from amino acid 46 to 2697; sequence coverage was 55%. The sequence of GT-8 mutant
405 fibrillin-1 is truncated at amino acid residue 1323. The sums of reporter ion intensities
406 (measurements of relative abundance) for the N-terminal region and the C-terminal region

407 of fibrillin-1 are shown for all genotypes in Figure 7A. The detection and signal response
408 of individual peptides in large-scale tryptic digests is a complicated process. All
409 genotypes showed lower intensity for C-terminal region fibrillin-1 peptide abundances
410 compared to N-terminal region (white bars versus black bars). The GT-8/+ and GT-8/H1Δ
411 aortic tissues had relatively greater reductions in C-terminal fibrillin-1 peptides compared
412 to wildtype, as expected since the C-terminal half of GT-8 truncated fibrillin-1 is missing.
413 There was also a very significant reduction (Figure 7B) in N-terminal fibrillin-1 peptides in
414 GT-8/H1Δ aorta compared to wildtype. Therefore, the reduced abundance of fibrillin-1 in
415 GT-8/H1Δ aorta compared to wildtype is not fully explained by the reduced C-terminal
416 intensity.

417 **Figure 7. Relative abundances of N-terminal and C-terminal fibrillin-1 peptides in**
418 **wildtype and *Fbn1* mutant ascending thoracic aortae.** A) Average total protein
419 reporter intensities of N-terminal fibrillin-1 peptides (black bars) and C-terminal fibrillin-1
420 peptides (white bars) are displayed for each genotype. B) Average intensities of N-
421 terminal and C-terminal peptides from each mutant genotype were compared to wildtype.
422 Significance was determined by two-tailed two-sample with equal variance t-test.

A



423

424 **B**

	Comparison	N-terminal p-value	C-terminal p-value
425	WT vs. GT-8/+	0.1260	0.0325
	WT vs. H1Δ/H1Δ	0,1068	0.2455
426	WT vs. H1Δ/+	0.0207	0.1051
	WT vs. GT-8/H1Δ	0.0039	0.0048

427

428 ***STRING-DB functional enrichment analyses reveal novel pathways in H1Δ***
 429 ***ascending aorta***

430 STRING-DB (<https://string-db.org/>) enrichment analyses were performed to reveal
 431 other potential pathways associated with ascending aortic tissues in the *Fbn1* mutant
 432 genotypes (Tables 3 and 4). The highest enrichment scores (5.5 in H1Δ/+ and 4.6 in
 433 H1Δ/H1Δ) were identified for “Regulation of angiotensin levels in blood and basement
 434 membrane disassembly” in H1Δ ascending aorta (Table 3). In contrast, pathways
 435 showing top common enrichment scores for GT-8/+ and GT-8/H1Δ were networks
 436 involving aromatic amino acid metabolism and glutathione transferase activity (Table 4).
 437 Both of these common pathways were decreased compared to wildtype. Networks
 438 involving collagen trimers were increased in GT-8/+ and decreased in GT-8/H1Δ. The
 439 highest enrichment scores for GT-8/+ were increased laminin networks and increased
 440 inflammation networks, while decreased microfibril networks were found in GT-8/H1Δ
 441 (Table 4). These STRING-DB analyses support the selection of extracellular matrix
 442 proteins shown in Tables 1 and 2. Illustrations of these enrichment pathways are shown
 443 in Supplementary Figure 4.

444

445 **Table 3. Functional enrichment analysis of H1Δ ascending aorta compared to**
 446 **wildtype aorta.** Top pathways found to be enriched (according to STRING-DB) in H1Δ
 447 aorta are listed, along with enrichment score, false discovery rate (FDR), and direction of
 448 enrichment (increase or decrease).

Network or Pathway	Enrichment score	FDR	Direction
<i>Common enrichments</i>			
Regulation of angiotensin levels in blood, and basement membrane disassembly	H1Δ/+ 5.5	0.0003	Increase
	H1Δ/H1Δ 4.6	0.004	Increase
DNA Damage/Telomere Stress Induced Senescence	H1Δ/+ 2.1	0.007	Increase
	H1Δ/H1Δ 2.5	0.004	Increase
H1Δ/+			
Cytosolic small ribosomal subunit	1.4	0.00005	Increase
Fatty acid binding	1.4	0.006	Decrease
H1Δ/H1Δ			
Striated Muscle Contraction, and Thick filament	2.2	0.004	Increase

449

450

451 **Table 4. Functional enrichment analyses of GT-8/+ and GT-8/H1Δ ascending aorta**
 452 **compared to wildtype aorta.** Top pathways found to be enriched (according to
 453 STRING-DB) are listed, along with enrichment score, false discovery rate (FDR), and
 454 direction of enrichment (increase or decrease).

Network or Pathway	Enrichment score		FDR	Direction
<i>Common enrichments</i>				
Aromatic amino acid family metabolic process, and pentose and glucuronate interconversions	GT-8/+	2.3	0.006	Decrease
	GT-8/H1Δ	3	0.003	Decrease
Crosslinking of collagen fibrils/complex of collagen trimers Fibrillar collagen trimer	GT-8/+	2	0.007	Increase
	GT-8/H1Δ	3.2	0.004	Decrease
Glutathione transferase activity, and glutathione peroxidase Hepoxilin biosynthesis/glutathione transferase activity	GT-8/+	2	0.002	Decrease
	GT-8/H1Δ	5.1	0.005	Decrease
GT-8/+				
Laminin interactions	2.2		0.0002	Increase
Inflammatory response pathway	2.2		0.002	Increase
GT-8/H1Δ				
Abnormal nucleotide metabolism	4.9		0.002	Decrease
Microfibril	3.8		0.000008	Decrease

455
 456 No extracellular matrix pathways were enriched in analyses of either H1Δ/+ or
 457 H1Δ/H1Δ proteomics data. However, the increases in the network associated with
 458 “regulation of angiotensin levels and basement membrane disassembly” in H1Δ
 459 ascending aorta were especially interesting. The relative abundances of four of the five
 460 proteins in this cluster were all increased in H1Δ/+ and H1Δ/H1Δ aortic tissues (Table 5).
 461 These increased proteins were all mast cell proteases.
 462

463 **Table 5. Mast cell proteases in ascending thoracic aorta of *Fbn1* mutant male mice.**
464 Average total protein reporter ion intensities, fold changes (%change), and Benjamini-
465 Hochberg adjusted p-values (FDR) relative to wildtype. Values under the protein name
466 are the approximate abundance rank in the data set (out of 2,721 proteins). The number
467 analyzed for each genotype is listed as n=2 or n=3. Standard deviations are listed in
468 parentheses below the average reporter ion intensities. The adjusted p-values for each
469 individual protein are not significant. Note: The FDR significance cutoff is 0.1 (rather
470 than 0.05). Shading was assigned according to fold change: none = fold change $\leq \pm 1.1$,
471 lightest shade = fold change $\pm 1.1 - \leq 1.3$, medium shade = fold change $\pm 1.3 - \leq 1.5$, and
472 darkest shade = fold change > 1.5 . Orange shading represents increased fold changes;
473 blue shading, decreased fold changes.

Protein	Wildtype (n=3)	H1Δ/+ (n=2)	H1Δ/H1Δ (n=2)	GT-8/+ (n=3)	GT-8/H1Δ (n=2)
Mast cell carboxypeptidase A (328)	524,199 (348,148)	897,563 (114,253) 1.71 (71%) p = 0.39	747,312 (16,363) 1.43 (43%) p = 0.88	446,102 (275,729) -1.18 (-15%) p = 0.99	499,996 (50,279) 1.05 (-5%) p = 0.95
Chymase (511)	347,207 (238,493)	565,539 (210,874) 1.63 (63%) p = 0.48	500,983 (28,227) 1.44 (44%) p = 0.88	269,998 (62,300) -1.28 (-22%) p = 0.98	284,881 (45,574) -1.22 (-18%) p = 0.79
Mast cell protease 4 (624)	217,938 (220,684)	443,856 (149,164) 2.04 (104%) p = 0.47	349,486 (22,918) 1.60 (60%) p = 0.90	166,901 (71,726) -1.32 (-24%) p = 0.99	220,480 (32,239) 1.01 (1%) p = 0.98
Tryptase beta-2 (1659)	36,688 (37,346)	76,704 (18,095) 2.09 (109%) p = 0.42	61,041 (6,930) 1.66 (66%) p = 0.88	25,641 (6,801) -1.43 (-30%) p = 0.98	44,253 (674) 1.21 (21%) p = 0.84

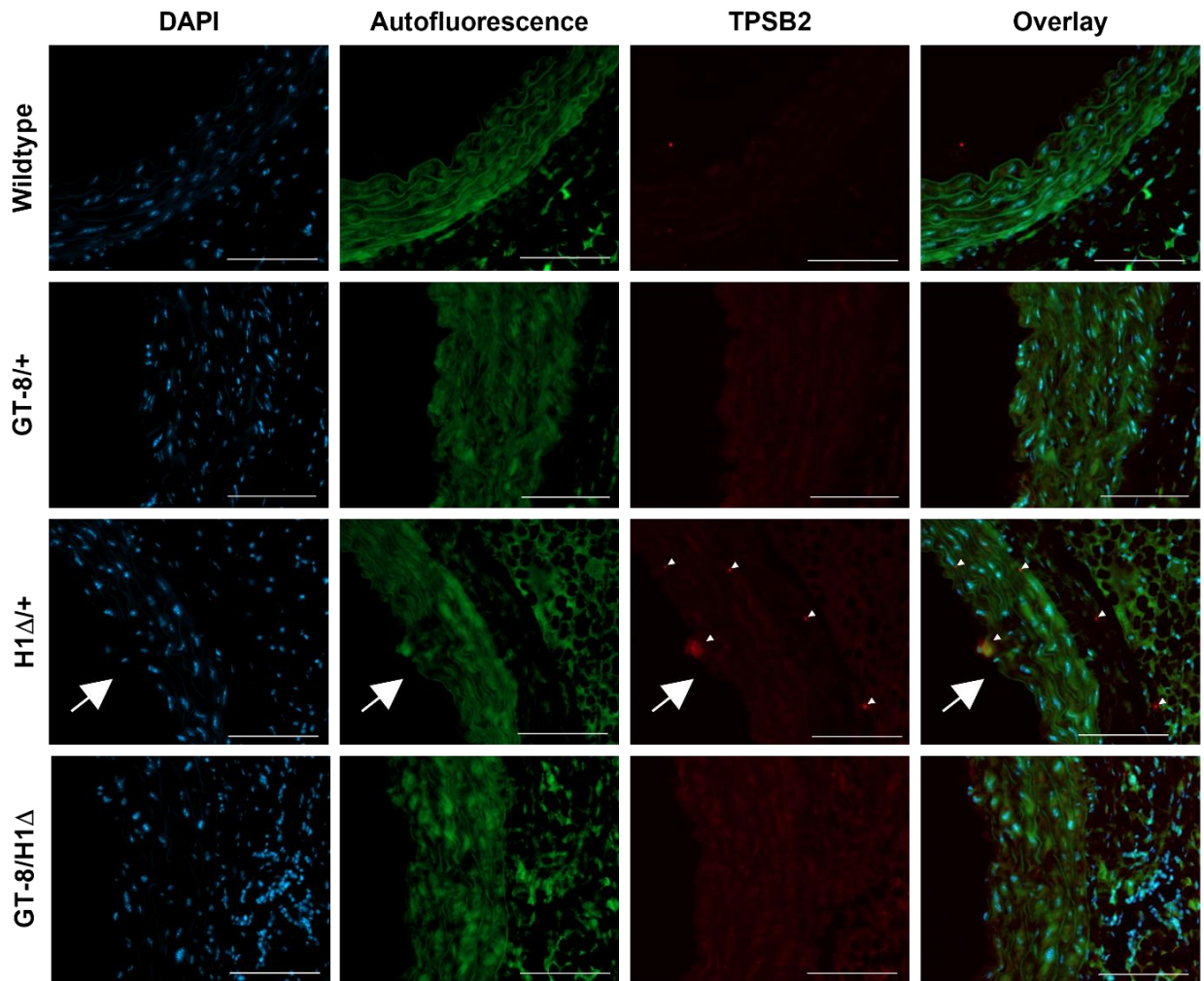
474

475

476 Individual p-values for these mast cell proteases did not reach significance.
477 Nevertheless, they were identified by STRING-DB pathway enrichment analyses. We
478 validated these findings using immunofluorescence microscopy. Mast cell protease
479 tryptase beta-2 was enriched in the ascending thoracic aorta of H1Δ/+ mice compared to
480 aorta from wildtype and other *Fbn1* mutants (Figure 8). Tryptase beta-2 was mostly
481 observed in the tunica media, especially in the area of microdissection.

482

483 **Figure 8. Immunostaining for tryptase beta-2 (TPSB2) mast cell protease in**
484 **ascending thoracic aorta of *Fbn1* mutant mice.** Representative images of ascending
485 aortic tissues from 6 month old male wildtype, GT-8/+, H1Δ/+, and GT-8/H1Δ mice. White
486 arrowheads indicate TPSB2-positive immunostaining. Microdissection in H1Δ/+ aortic
487 tissue is indicated by a white arrow. *Overlay of DAPI (blue) and TPSB2 (red) staining is
488 displayed along with the autofluorescence signal of elastin (green). Scale bars = 100 μm.



489

490

491

492 **DISCUSSION**

493 Abnormal TGF β signaling has been proposed to be the main driver of disease in
494 MFS [14]. However, the exact role of TGF β signaling in thoracic aortic disease remains
495 elusive [24]. Initial studies suggested that excess activation of TGF β , due to fibrillin-1
496 deficiency and consequent loss of binding of large latent TGF β complexes to fibrillin-1,
497 resulted in multiple MFS-related manifestations including emphysema [7], mitral valve
498 prolapse [8], aortic dilation [9], and skeletal muscle damage [10]. Subsequent studies
499 have shown an important protective effect for TGF β signaling in aortic tissue, at least in
500 early stages of disease [15]. In our study, we addressed the complex roles of TGF β
501 signaling in thoracic aortic disease by taking advantage of *Fbn1* mutant mouse models
502 that represent mild, moderate, and severe disease and employing both quantitative
503 (isobaric labeling proteomics) and qualitative (pSMAD2 immunostaining) measures to
504 assess TGF β signaling. Our data contribute to several important areas of current interest:
505 TGF β isoforms in aortic disease, the structural and regulatory roles of fibrillin-1, and
506 extracellular matrix proteins in aneurysm and in dissection or rupture.

507 ***TGF β isoforms in thoracic aortic disease***

508 Most studies investigating the role of TGF β signaling in the pathogenesis of
509 thoracic aortic pathology do not discriminate between the homologous isoforms of TGF β .
510 To gain more insight into the physiological role of these isoforms in MFS-associated
511 aortopathy, we used a mouse genetic approach to determine the effects of reduced
512 expression of *Tgfb1* and *Tgfb2* within the context of an *Fbn1* mutant mouse model (GT-
513 8/+) that develops aortic aneurysm.

514 We found clear isoform-specific effects of TGF β on aortic disease. Aortic disease
515 severity in GT-8/+ mice was amplified by reducing the expression of *Tgfb2*. Most
516 importantly, half of the GT-8/Tgf β 2 mice died by the age of 8 months old from aortic
517 rupture. In contrast, GT-8/+ mice haploinsufficient for *Tgfb1* showed no difference in
518 survival compared to wildtype. A recent study of doubly mutant *Tgfb2*^{+/-};*Fbn1*^{mgR/mgR} mice
519 also reported that reduced *Tgfb2* expression resulted in a more severe aortic phenotype
520 and increased mortality compared to *Fbn1*^{mgR/mgR} mice [25]. Moreover, findings in
521 humans support an isoform-specific effect of TGF β in aortic disease. We and others have
522 identified *TGFB2* pathogenic variants in patients with syndromic and non-syndromic
523 forms of thoracic aortic aneurysms and dissections [21,26,27]. In accord with these
524 results, our proteomics analyses of aortic tissues in mouse models identified TGF β 2 as
525 the only quantifiable TGF β isoform. These studies are consistent with the finding of a
526 requirement for TGF β 2 in the development of the aorta [19].

527 Interestingly, reduced *Tgfb1* expression in GT-8 mice led to decreased aortic root
528 diameters compared to single mutant GT-8/+ mice, but not to wildtype mice. Studies in
529 *Tgfb2*^{+/-};*Fbn1*^{C1039G/+} mice and in humans with *TGFB2* variants have revealed
530 upregulation of *Tgfb1* and *TGFB1* in the ascending aorta, suggesting compensation by
531 *TGFB1* when *TGFB2* is reduced. This compensation may lie behind the “paradoxical”
532 increase in TGF β signaling as measured by pSMAD2 immunostaining [21]. Additional
533 investigations of a role for TGF β 1 in the pathogenesis of thoracic aortic disease are
534 warranted.

535 ***Structural and regulatory roles of fibrillin-1***

536 In this study, we also aimed to reveal the consequences for aortic disease of
537 deleting the binding site in fibrillin-1 for large latent TGF β complexes. Here, we used our
538 mouse genetic approach to compare the effects of deletion of the first hybrid domain of
539 fibrillin-1 with reduction of *Tgfb1* or *Tgfb2* within the context of GT-8/+, our *Fbn1* mutant
540 mouse model with aneurysm. This approach allowed us to compare over time the effects
541 of reduced expression of TGF β isoforms with deletion of the LTBP binding site on
542 aneurysm development. Aortic disease severity in GT-8/+ mice was amplified by
543 replacing the wildtype *Fbn1* allele with the H1 Δ allele. Survival curves, ultrasound
544 measurements of aortic dimensions, and aortic wall morphology all demonstrated a
545 similar increase in severity of aortic disease, when we compared GT-8/H1 Δ with GT-
546 8/Tgf β 2 mice.

547 This study shows that fibrillin-1, in which the first hybrid domain is deleted in-frame,
548 cannot replace the function of wildtype fibrillin-1, even though the structural function of
549 assembling fibrillin microfibrils appeared normal in H1 Δ /+ and H1 Δ /H1 Δ mice [18].
550 Synchrotron microCT imaging conclusively demonstrated that, even though ultrasound
551 and conventional histology failed to establish an aortic disease phenotype, the ascending
552 aorta of H1 Δ /+ mice contained regions of microdissection, characterized by major breaks
553 in the elastic lamellae. Quantitative proteomics analyses of ascending aorta from both
554 H1 Δ /+ and H1 Δ /H1 Δ mice showed reduced amounts of LTBP-1, LTBP-3, and LTBP-4
555 present in these tissues compared to wildtype. However, LTBP-3 and LTBP-4 were not
556 absent as has been suggested from immunofluorescence analyses of *Fbn1* null tissues
557 [28]. It is possible that these LTBPs, like LTBP-1 [28], may interact with other molecules
558 that also bind to fibrillin. These molecules include fibronectin [28] and the short fibulins

559 [17], and potentially other molecules that all together form the multimolecular microfibril.
560 Moreover, only one domain in fibrillin-1 is missing in H1 Δ mice, leaving the rest of the
561 molecule to participate in multimolecular matrix interactions. Quantitative proteomics
562 analyses showed no differences in amounts of fibronectin and fibulins -3, -4, and -5
563 between H1 Δ aorta and wildtype.

564 Instead of a matrix structural deficit, as found for example in *Fbn1* null tissues, our
565 study suggests that the regulatory function of fibrillin-1 may be compromised when the
566 first hybrid domain is deleted, since quantitative proteomics analyses of ascending aorta
567 from H1 Δ /+ and H1 Δ /H1 Δ mice revealed not only reduced amounts of LTBP-1, LTBP-3,
568 and LTBP-4, but also reduced amounts of TGF β 2, and of the TGF β signaling readouts
569 collagen I, collagen III, and PAI-1. Although each of these individual changes were not
570 statistically significant when compared to the matched individual wildtype proteins, the
571 combined trend suggests a profile of reduced TGF β signaling in H1 Δ /+ and H1 Δ /H1 Δ
572 mice. This profile of reduced TGF β signaling was supported by immunofluorescent
573 staining for pSMAD2, which was reduced in H1 Δ /+ aorta compared to the other
574 genotypes. Moreover, we found that the most prominently enriched pathway revealed in
575 these mice was one composed of four mast cell proteases. Both mast cell chymase and
576 mast cell tryptase have been implicated in the pathogenesis of human and mouse
577 abdominal aortic aneurysms [29, 30]. Because it is known that TGF β signaling can both
578 inhibit as well as augment mast cell functions [31], we speculate that, in H1 Δ /+ ascending
579 aorta, local environments in which TGF β signaling is reduced might be permissive for the
580 expansion of mast cells and release of mast cell proteases, resulting in the local
581 degradation of elastic lamellae.

582 It is well established that total loss of fibrillin-1 in *Fbn1*^{-/-} mice and pronounced
583 fibrillin-1 deficiency in *Fbn1*^{mgR/mgR} result in thoracic aortic rupture and early death.
584 Quantitative proteomics revealed a significant reduction in fibrillin-1 peptides in GT-8/H1Δ
585 aorta compared to wildtype (Table 2). It is likely that the marked reduction in fibrillin-1
586 contributes to thoracic aortic rupture observed in GT-8/H1Δ mice. To gain additional
587 insight into the reduction of fibrillin-1 peptides in GT-8/H1Δ mice, the relative abundance
588 of peptides in the N-terminal half of fibrillin-1 was compared to peptides in the C-terminal
589 half in all genotypes (Figure 7), and as expected, both GT-8/+ and GT-8/H1Δ aortic
590 tissues contained significantly fewer C-terminal peptides, consistent with the engineered
591 truncation of GT-8 fibrillin-1. However, a significant reduction in N-terminal peptides was
592 found in GT-8/H1Δ, but not in GT-8/+, aortic tissues. Therefore, it is likely that the
593 reduction in fibrillin-1 peptides in GT-8/H1Δ ascending aorta is due to mechanisms
594 beyond the structural effects of the engineered mutations on fibrillin-1. In addition, since
595 *Fbn1*^{+/-} mice do not die from aortic rupture, it is also likely that reduction in fibrillin-1 is not
596 the sole cause of aortic rupture in GT-8/H1Δ mice.

597 ***Extracellular matrix proteins in aneurysm and in dissection or rupture***

598 The use of both a mouse genetic approach and quantitative proteomics analyses
599 of *Fbn1* mutant mouse models of aneurysm (GT-8/+), of aneurysm and rupture (GT-
600 8/H1Δ), and of microdissection (H1Δ/+) allowed us to identify clear molecular differences
601 between these models, including differences in TGFβ signaling components, classical
602 readouts for TGFβ signaling, and in extracellular matrix composition and organization.
603 Our working hypothesis is that reduced TGFβ signaling may be associated with
604 microdissection in H1Δ, whereas increased TGFβ signaling is associated with aneurysm

605 in GT-8. Pathway analyses for proteins in H1 Δ /+ and H1 Δ /H1 Δ ascending aorta revealed
606 enrichment of mast cell proteases but no enrichment of extracellular matrix pathways. In
607 contrast, proteins in GT-8/+ ascending aorta were grouped into multiple extracellular
608 matrix pathways all showing increased abundance compared to wildtype. These
609 increases in extracellular matrix pathways likely reflect increased TGF β signaling, even
610 though pSMAD2 immunostaining in GT-8/+ aorta was similar to wildtype. Indeed, most
611 of the extracellular matrix proteins found to be increased in GT-8/+ ascending aorta are
612 known to be direct targets of TGF β signaling [23].

613 Comparison of GT-8/H1 Δ proteomics results and enrichment analyses with those
614 of GT-8/+ is complex. While analyses of GT-8/+ aortic proteins showed increases in
615 multiple extracellular matrix pathways, analyses of GT-8/H1 Δ aortic proteins showed
616 specific marked reductions in microfibril and collagen pathways and both increases as
617 well as reductions in multiple other extracellular matrix pathways. Quantitative
618 proteomics analyses indicated that versican and MFAP-4 are significantly reduced, and
619 fibronectin is significantly increased, as initial steps in 4 month old GT-8/+ aneurysm
620 progression. This profile was also found in GT-8/H1 Δ aneurysm that is beyond initial
621 development and is already proceeding toward rupture. However, in addition, there were
622 significant reductions in GT-8/H1 Δ in other extracellular matrix proteins: fibrillin-1, fibrillin-
623 2, MAGP-1, LRC-17, collagen VI, and LTBP-4. Reductions in microfibrillar proteins may
624 serve to signal events leading to rupture, compared to events leading to aneurysm.
625 Indeed, the highest levels of circulating fibrillin-1 [32] and fibrillin-2 [33] fragments in
626 human plasma were found in individuals with (non-genetic forms of) thoracic aortic

627 aneurysm and dissection, suggesting that these proteomics analyses of *Fbn1* mutant
628 mice may be relevant to human aortic disease in the general population.

629 We hypothesize that the molecular events associated with the reductions in
630 extracellular matrix in GT-8/H1 Δ ascending aorta will reveal critical pathways leading to
631 aortic dissection and rupture. These unknown critical pathways may be caused by
632 detrimental increased TGF β signaling. Increased TGF β signaling has clearly been
633 demonstrated in patients with MFS with advanced aortic disease, since samples are
634 obtained from patients undergoing surgical intervention. In GT-8/H1 Δ aorta, our model
635 of severe aortic disease, pSMAD2 immunofluorescence indicated increased TGF β
636 signaling, in accord with the increased abundance of SMAD2 found by proteomics. In
637 contrast, although increased aortic pSMAD2 staining was reported during early disease
638 development in MFS C1039G/+ mice [9], our pSMAD2 immunostaining of GT-8/+ aortic
639 tissues did not reveal any statistically significant increase compared to wildtype. But, our
640 proteomics analyses indicated notable increases in extracellular matrix molecules and
641 pathways, which could serve as evidence for increased TGF β signaling. Our results
642 support the previously reported dimorphic effects of TGF β signaling in aortic disease,
643 shown when TGF β neutralizing antibodies administered early led to exacerbated effects
644 on aortic disease and mitigating effects, when administered after aneurysm formation
645 [15]. In our study as well as in the previous study [15], the specific molecular mechanisms
646 mediated by TGF β signaling in aneurysm development and in rupture remain for future
647 investigation.

648 **Conclusion**

649 TGF β signaling is well known to be context dependent [34]. Our studies indicate
650 that fibrillin-1 microfibrils perform important regulatory roles influencing the extracellular
651 context for TGF β signaling [35]. However, the precise molecular mechanisms by which
652 alterations in the fibrillin-1 matrix results in reduced or increased TGF β signaling cannot
653 be easily teased apart, without substantial contrivance and artificial manipulation,
654 because the extracellular matrix is designed to hang together. Hence, although the LTBP
655 binding site is deleted in H1 Δ /+ and H1 Δ /H1 Δ , LTBPs are clearly present in the aortic
656 tissue of these mice, likely because LTBPs also interact with other matrix molecules. The
657 fibulins and Adamts-like proteins, which interact with fibrillin-1 in sites close to the LTBP
658 binding site, may also play roles in the matrix context of TGF β signaling. In spite of this
659 imprecision in molecular mechanisms governing fibrillin-1 matrix control of TGF β
660 signaling, we propose that our findings make significant contributions to understanding
661 the roles of TGF β signaling in aortic disease. Our novel *Fbn1* mutant mouse models of
662 microdissection (H1 Δ /+) and of aortic aneurysm-with-rupture (GT-8/H1 Δ) can now be
663 added to models of aortic aneurysm-without-rupture (GT-8/+ and C1039G/+) to span the
664 full range of mild to severe aortic disease. Our ongoing studies of disease *progression*
665 *over time* associated with these stages of aortic disease may reveal how TGF β signaling
666 specifically contributes to each of these stages and interfaces with other molecular
667 pathways of pathogenesis.

668 ***Limitations***

669 A major limitation of our study is that only male mice were analyzed. We chose to
670 restrict our study to males because we previously showed that female GT-8/+ mice did
671 not demonstrate comparable enlargement of aortic diameters or severity of aortic

672 histology [20]. In the future, we aim to extend our investigations to include analyses of
673 female mice. It is also important to acknowledge that our studies did not investigate the
674 role of reduced *Tgfb3*, within the context of our aneurysm *Fbn1* mutant mouse model.
675 There is evidence today that mutations in *TGFB3* are associated with thoracic aortic
676 aneurysm [36]. However, TGFβ3 was not present in our mouse aorta proteomics
677 database, and heterozygous loss of *Tgfb3* in *Fbn1*^{mgR/mgR} mice has been reported not to
678 have any effect on the survival of these mice [25]. Lastly, our study focused on
679 pathophysiology associated with the ascending thoracic aorta. Investigations of aortic
680 disease pathologies across different segments of the aorta, from the root to the arch,
681 might lead to a better, more comprehensive understanding of the underlying mechanisms
682 of aortic disease in MFS.

683

684 **EXPERIMENTAL PROCEDURES**

685 *1. Animals*

686 All experiments on mice were carried out in strict accordance with the
687 recommendations in the Guide for the Care and Use of Laboratory Animals of the National
688 Institutes of Health. The protocols were approved by the Oregon Health & Science
689 Institutional Animal Care and Use Committee (Permit Number: ISO1405) and the Ethics
690 Committee on Laboratory Animal Experiments at the Faculty of Medicine of Ghent
691 University (Permit Number: ECD 18-24). All efforts were made to minimize suffering.
692 Experiments were performed with male mice. Wildtype littermates were used as controls
693 unless otherwise specified.

694 Details of the generation of GT-8/+ and H1Δ/H1Δ mice were described previously
695 [18]; these strains were produced on a pure C57BL/6J background. Double heterozygous
696 mutant mice were generated by crossing GT-8/+ mice with heterozygous *Tgfβ1*^{+/-} knock-
697 out mice (JAX stock #002220; C57Bl/6J background), heterozygous *Tgfβ2*^{+/-} knock-out
698 mice (JAX stock #003102; mixed 129/Sv;C57Bl/6J background) [19], or homozygous
699 H1Δ/H1Δ mice. Polymerase chain reaction-based genotyping was performed as
700 previously described for the GT-8/+ and H1Δ/H1Δ mice [18]. *Tgfβ1*^{+/-} and *Tgfβ2*^{+/-} knock-
701 out mice were genotyped according to JAX guidelines. Experimental GT-8/Tgfβ2 and
702 GT-8/Tgfβ1 mice were F1 generation offspring with littermate controls.

703 Mice survival was assessed until 8 months of age. Number of mice enrolled in the
704 survival study: n = 9 GT-8/+; n = 7 H1Δ/+; n = 9 GT-8/Tgfβ1; n = 17 GT-8/Tgfβ2; n = 9
705 GT-8/H1Δ.

706 2. Cardiovascular ultrasound

707 All cardiovascular ultrasound studies were performed under general anesthesia (1
708 - 1.5% isoflurane mixed with 0.5 L/min 100% O₂) using a Vevo 2100 (Visualsonics)
709 instrument equipped with a high-frequency linear array transducer (MS 550D, frequency
710 22-55MHz). The number of animals included at 6 months of age: n = 10 wildtype (*Tgfβ1*^{+/-}
711 cross); n = 16 wildtype (*Tgfβ2*^{+/-} cross); n = 10 GT-8/+ (*Tgfβ1*^{+/-} cross); n = 10 GT-8/+
712 (*Tgfβ2*^{+/-} cross); n = 10 *Tgfβ1*^{+/-}; n = 10 *Tgfβ2*^{+/-}; n = 13 GT-8/Tgfβ1; n = 10 GT-8/Tgfβ2; n
713 = 7 H1Δ/+; n = 6 GT-8/H1Δ.

714 Since the GT-8/Tgfβ1 strain was on a pure C57BL/6J genetic background, the
715 wildtype littermates were used as controls for cardiovascular ultrasound analyses of GT-
716 8/H1Δ mice that were F1 generation offspring of the GT-8/+ and H1Δ/H1Δ cross.

717 Mouse heart rate and respiration were evaluated during the entire procedure.
718 Aortic dimensions were measured at end diastole from inner-to-inner edge at the level of
719 the sinuses of Valsalva, proximal and distal ascending aorta, transverse arch and
720 descending thoracic aorta. Main pulmonary artery dimensions were also measured.
721 Ultrasound images were analyzed by one individual blinded to the genotype.

722 *3. Histological and immunofluorescent staining*

723 Histological studies were performed on the aortic root as previously described [20].
724 Mice were sacrificed by CO₂ overdose (1.0L/min) and cervical dislocation. Aortae were
725 fixed in cacodylate buffered 1.5% glutaraldehyde/1.5% paraformaldehyde containing
726 0.05% tannic acid (w/v), rinsed, exposed to 1% osmium tetroxide, then dehydrated in a
727 graded series of ethanol to 100%. Tissue was rinsed in propylene oxide and embedded
728 in Spurr's epoxy. One micron thick sections of the aortic root were stained with toluidine
729 blue and basic fuchsin. Alternatively, two micron sections were mounted on glass slides
730 stained as described in Van Reempts and Borgers, 1975 [37]. Stained sections were
731 examined on a Leica DMIRE2 inverted microscope and photographed using a top
732 mounted Q Imaging Micropublisher with Q Capture Pro software. The number of animals
733 included at 6 months of age: n = 10 wildtype; n = 2 GT-8/+; n = 4 *Tgfβ1*^{+/-}; n = 1 *Tgfβ2*^{+/-}
734 ; n = 3 GT-8/*Tgfβ1*; n = 3 GT-8/*Tgfβ2*, and at 8 months of age: n = 7 wildtype ; n = 5 GT-
735 8; n = 4 H1Δ/+; n = 7 GT-8/H1Δ. The number of animals for end-stage aortic disease
736 analysis: n = 3 GT-8/H1Δ; n = 1 GT-8/*Tgfβ2*.

737 Histological studies were also performed on the ascending aorta of mice. The
738 number of male mice included at the age of 6 months: n = 5 wildtype; n = 6 GT-8/+; n =
739 6 H1Δ/+; n = 4 GT-8/H1Δ. Mice were sacrificed by CO₂ overdose (1.0L/min), and aortae

740 were fixed overnight in 4% paraformaldehyde (PFA) at 4°C, followed by dehydration and
741 paraffin embedding using a Leica TP1020 tissue processor. Subsequently, 5 µm thick
742 cross sections of the ascending aorta were obtained using a Microm HM35ss microtome.
743 Tissues were deparaffinized and rehydrated before staining with hematoxylin-eosin
744 (H&E), Weigert's Resorcin Fuchsin (to stain elastin), and picro-sirius red (PSR, to stain
745 collagen). Stained sections were visualized on a Zeiss Axio Observer.Z1 microscope
746 coupled to an Axiocam camera. To obtain an overview image of the entire aortic tissue
747 cross-section, stitching algorithms of Zeiss ZEN Pro software were used. All micrographs
748 were analyzed to count fragmentation and major breaks [20]. Major breaks were defined
749 as elastic fiber breaks that spanned ≥ 3 layers of elastic lamellae. The number of major
750 breaks were counted per whole aortic cross-section by one individual blinded to the
751 genotype.

752 For TPSB2 immunofluorescent staining, heat-induced antigen-retrieval with tris-
753 buffered saline with 0.05% Tween 20 (TBST buffer) using a pressure cooker (2100
754 Retriever, Laborimpex – BaseClear Lab Products) was used to unmask epitopes of
755 interest. Next, sections were washed three times in distilled water. Subsequently,
756 nonspecific binding was blocked by incubation with 5% bovine serum albumin (BSA) in
757 TBST buffer for 1 hour at room temperature. Tryptase beta-2 was detected by overnight
758 incubation at 4°C in a humidified chamber with a rabbit TPSB2 polyclonal antibody (PA5-
759 121532; Fisher Scientific) diluted 1/100 in TBST buffer containing 5% BSA. Next,
760 sections were incubated for one hour at room temperature in a dark humidified chamber
761 with DyLight™ 633 goat anti-rabbit IgG (H + L) diluted 1/1000 in TBST buffer containing
762 5% BSA. Afterwards, anti-fade mounting medium with DAPI (H-1200, Vectashield) was

763 used to mount and coverslip the sections. Stained sections were visualized on a Zeiss
764 Axio Observer.Z1 microscope coupled to an Axiocam camera.

765 For pSMAD2 immunofluorescent staining, heat-induced antigen-retrieval with 1M
766 Tris-EDTA with 0.05% Tween 20 (pH 9) for pSMAD2, using a warm water bath at 90°C
767 for 45 minutes, unmasked epitopes. Next, sections cooled down for 20 minutes and were
768 washed three times in TBST buffer. Subsequently, free aldehyde groups were blocked
769 by incubation with 50 mM Ammonium Chloride (pH 7.4) for 20 minutes, and sections were
770 permeabilized using 0.1% Triton X-100 for 10 minutes. Thereafter, nonspecific binding
771 was blocked by incubation with 5% BSA in TBST buffer for 1 hour at room temperature.
772 pSMAD2 was detected by overnight incubation at 4°C in a humidified chamber with a
773 rabbit Anti-SMAD2 (phospho S467) recombinant monoclonal antibody (EPR23681-40)
774 (1:50 dilution, ab280888; ABCAM) in TBST buffer containing 5% BSA. Next, sections
775 were incubated for one hour at room temperature in a dark humidified chamber with
776 DyLight™ 633 goat anti-rabbit IgG (H + L) diluted 1/1000 in TBST buffer containing 5%
777 BSA. Afterwards, anti-fade mounting medium with DAPI (H-1200, Vectashield) was used
778 to mount and coverslip the sections. Stained sections were visualized on a Zeiss Axio
779 Observer.Z1 microscope coupled to an Axiocam camera. To obtain an overview image
780 of the entire aortic wall cross-section, stitching algorithms of Zeiss ZEN Pro software were
781 used. The percentage of pSMAD2-positive nuclei were calculated semi-automatically per
782 whole aortic cross-section using Image J software, by one individual blinded to the
783 genotype.

784 *4. Synchrotron imaging*

785 Propagation-based phase-contrast synchrotron X-ray imaging was performed at
786 the TOMCAT (X02DA) beamline of the Swiss Light Source (Paul Scherrer Institute in
787 Villigen, Switzerland). PFA fixed aortic tissue samples (stored in 1x PBS buffer) were
788 immobilized in 1.5 mL Eppendorf tubes filled with low-melt agarose gel, which were fixed
789 onto the robot sample holder using wax. Settings related to the beamline (21.8 keV
790 monochromatic beam energy) and tomography scan (250 mm object-detector distance,
791 1501 projections, LUAg:CE 20 μm scintillator UPLAPO 4x objective, PCO.Edge 5.5
792 camera) were optimized for these tissue samples [38]. The tomographic reconstruction
793 into image stacks, including phase retrieval, was performed onsite using Paganin's
794 algorithm [39]. Image stacks of 2560 x 2560 pixels and 2160 slices were obtained at an
795 isotropic voxel size of 1.625 μm^3 . A field-of-view of 4.16 x 4.16 mm² (in plane) x 3.51 mm
796 (axial) was obtained. Image processing was performed using the medical software
797 package MIMICS[®]24.0 (Materialise). Image stacks were semi-automatically segmented
798 using the 'mask', 'segmentation tools', 'multiple slice edit', and 'interpolation tools', as
799 previously described [38]. Segmentation of the aortic wall structure was performed using
800 a conventional thresholding approach based on gray value differences. Finally, 3-D
801 reconstruction was created based on these masks.

802 *5. Proteomics*

803 *5.1. Sample preparation*

804 Dissected mouse ascending aorta tissues, from root to arch, were stored in 1.5 ml
805 polypropylene centrifuge tubes at -80°C until homogenization. Samples were thawed at
806 room temperature and washed four times with 200 μL of 1x PBS buffer. Tissue samples
807 were suspended in 200 μL of 5% SDS, 50 mM TEAB pH 8, and homogenized using a

808 Model 60 ultrasonic dismembrator (Fisher Scientific, Waltham, MA). Samples were kept
809 in an ice bath during homogenization with a 30 second rest in ice bath between ultrasonic
810 tissue disruption cycles. Homogenization used bursts of quickly increased power,
811 typically lasting 1-2 seconds, to keep the tissue and buffer from splashing out of the tube.
812 After an initial set of 5 power bursts, the sample tubes were incubated at 95°C for 5
813 minutes to denature large structural proteins. Homogenization steps continued until no
814 pieces of the mouse aorta were any longer visible. Samples were centrifuged at 5,000 x
815 g for five minutes; the filtrate was transferred to a 1.5 mL of LoBind centrifuge tube
816 (Eppendorf, Enfield, CT), and a Pierce BCA protein assay (ThermoFisher Scientific,
817 Waltham, MA) was performed.

818 A volume equal to 30 µg of protein from each sample was transferred to 1.5 ml
819 Lobind centrifuge tubes, and SDS protein extraction buffer (5% SDS, 50mM TEAB, pH8)
820 was added to bring the final volume to 75 µl. Samples were reduced by adding 3.4 µl of
821 0.5M dithiothreitol and incubated at 95°C for 10 min. Samples were alkylated by the
822 addition of 6.8 µl of 0.5M iodoacetamide and incubation at room temperature for 30 min
823 in the dark. Samples were then acidified by the addition of 8.5 µl of 12% phosphoric acid,
824 and 562 µl of SDS protein extraction buffer (90% aqueous methanol, 100 mM TEAB, pH
825 8) was added. Samples were transferred 165 µl at a time to S-trap micro columns (Protifi,
826 Farmingdale, NY) and inserted into 1.5 ml of polypropylene tubes. Samples were
827 centrifuged at 4,000 x g for 3 min between each addition of the sample. S-trap columns
828 were washed 6x using 160 µl 90% methanol, 100 mM TEAB followed by centrifugation at
829 4,000 x g for 3 min between each wash step. S-trap columns containing the bound
830 sample proteins were transferred to 1.5 ml Lobind centrifuge tubes and 40 µl of 80 ng/µl

831 sequencing grade modified trypsin (Promega, Fitchburg, WI, Cat # V5111) in 50 mM
832 TEAB was added. S-trap columns were capped, and digestion was performed at 37°C
833 overnight in a humidified chamber.

834 After digestion, peptides were eluted by sequential addition of 40 µl of 50mM
835 TEAB, 40 µl of 0.2% aqueous formic acid, and 40 µl of 50% acetonitrile, 0.2% formic acid,
836 with centrifugation at 4,000 x g for 4 min between each addition of elution buffer. The
837 eluted fractions were pooled and then dried by vacuum centrifugation, 100 µl of 50%
838 methanol added, and samples again dried. Samples were reconstituted with 100 µl of
839 water at 37°C in a shaker and peptide concentrations determined using a Pierce
840 Quantitative Colorimetric Peptide Assay (ThermoFisher Scientific, Cat # 23275). Seven
841 µL aliquots were removed from seven male samples with the highest recovery after the
842 digestion. These aliquots were pooled together to form the internal reference standard
843 samples used for internal reference scaling (IRS) data analysis [40]. For the TMTpro
844 labeling step described below, 10 µg of the peptide from each mouse aorta sample and
845 the common pool samples were dried by vacuum centrifugation. Dried peptides were
846 reconstituted by adding 20 µL of 100mM TEAB and shaking at 37°C for 15 minutes.

847 *5.2. TMTpro labeling and normalization run*

848 Two tandem mass tag (TMTpro) 16-plex reagent kits (ThermoFisher Scientific, Cat
849 # 90309) were used to label the digested mouse aorta peptide samples and pooled
850 standards. There were 12 male mice samples in each plex, respectively. Each plex had
851 duplicate channels of the pooled standard mixture so that samples between the plexes
852 could be compared. Each TMTpro 16-plex reagent (200ug) dissolved in 12ul of
853 anhydrous acetonitrile was added to 10ug of peptide sample in 20ul of 100mM TEAB,

854 and labeling performed by shaking at room temp for 1h. After the incubation, 2 μ l of each
855 labeled peptide digest were combined; 2 μ l of 5% hydroxylamine added, and samples
856 incubated at room temp for 15 min, then dried by vacuum centrifugation. The remaining
857 30 μ l of each labeled sample was frozen at -80°C without hydroxylamine addition, in case
858 relabeling was required.

859 The 2 μ l of each combined TMTpro labeled sample was then dissolved in 20 μ l of
860 5% formic acid and 2 μ g of peptides analyzed by a single 140 min LC-MS/MS method
861 using an Orbitrap Fusion Mass Spectrometer, as described below. These single LC runs
862 were performed to check labeling efficiency (typically >90%), and volumetrically adjust
863 each sample to provide similar total reporter ion intensities for each labeled sample in the
864 final combined sample for the 2D-LC/MS analysis. The remaining 30 μ l portion of each
865 TMTpro labeled sample was then thawed and aliquots were removed, based on the
866 calculated normalization factors that would produce 40 μ g of total peptides from all 16
867 samples in each plex (2.8 μ g of digest from each sample). To quench the labeling
868 reaction, 5% hydroxylamine was added to bring the total hydroxylamine concentration to
869 0.5% followed by incubation for 15 min at room temperature. The remaining labeled
870 peptides not used for the 2D-LC/MS were stored at -80°C in case a second run was
871 needed.

872 *5.3. Two-dimensional liquid chromatography/mass spectrometry (2D-LC/MS) analysis*

873 The multiplexed mouse aorta samples were dissolved in 10 mM ammonium
874 formate, pH9 buffer and injected onto a NanoEase 5 μ m XBridge BEH130 C18 300 μ m x
875 50 mm column (Waters Corporation, Milford, MA) at 3 μ l/min in a mobile phase containing
876 10 mM ammonium formate (pH 9). Peptides from mouse aortas were eluted by sequential

877 injection of 20 µl volumes of 17, 20, 21, 22, 23, 24, 25, 26, 27, 28, 29, 30, 35, 40, 50, 90%
878 ACN (16 fractions).

879 Eluted peptides were diluted at a 3-way union with mobile phase containing 0.1%
880 formic acid at a 24 µl/min flow rate and delivered to an Acclaim PepMap 100 µm x 2 cm
881 NanoViper C18, 5 µm trap (Thermo Fisher Scientific) on a switching valve. After 10 min
882 of loading, the trap column was switched on-line to a PepMap RSLC C18, 2 µm, 75 µm x
883 25 cm EasySpray column (ThermoFisher Scientific). TMTpro 16-plex labeled peptides
884 from mouse aortas were then separated at low pH in the second dimension using a 5–
885 25% ACN gradient over 100 min in the mobile phase containing 0.1% formic acid at a
886 300 nL/min flow rate.

887 Tandem mass spectrometry data was collected using an Orbitrap Fusion Tribrid
888 instrument configured with an EasySpray NanoSource (Thermo Scientific, San Jose, CA).
889 Survey scans were performed in the Orbitrap mass analyzer at resolution = 120,000, with
890 internal mass calibration enabled, and data-dependent MS2 scans using dynamic
891 exclusion performed in the linear ion trap using collision-induced dissociation. Reporter
892 ion detection was performed in the Orbitrap mass analyzer using MS3 scans following
893 synchronous precursor isolation of the top 10 ions in the linear ion trap, and higher-energy
894 collisional dissociation in the ion-routing multipole. Full instrument parameters are in
895 Supplementary Table 1. There were 285,288 sets of instrument scans acquired for the
896 male plex.

897 *5.4. Data analysis*

898 Proteome UP000000589 (mouse, taxon ID 10090) canonical FASTA sequences
899 (20,002 proteins) were downloaded September 2021 from www.UniProt.org. Common

900 contaminants (174 sequences) were added, and sequence-reversed entries were
901 concatenated for a final protein FASTA file of 44,352 sequences.

902 The 32 binary instrument files (16 fractions in each of the two plexes) were
903 processed with the PAW pipeline [41]. Binary files were converted to text files using
904 MSConvert [42]. Python scripts extracted TMTpro reporter ion peak heights and fragment
905 ion spectra in MS2 format [43]. The Comet search engine (version 2016.03) [44] was
906 used: 1.25 Da monoisotopic peptide mass tolerance, 1.0005 Da monoisotopic fragment
907 ion tolerance, fully tryptic cleavage with up to two missed cleavages, variable oxidation of
908 methionine and proline residues, static alkylation of cysteines, and static modifications for
909 TMTpro labels (at peptide N-termini and at lysine residues).

910 Top-scoring peptide spectrum matches (PSMs) were filtered to a 1% false
911 discovery rate (FDR) using interactive delta-mass and conditional Peptide-prophet-like
912 linear discriminant function [45] scores. Incorrect delta-mass and score histogram
913 distributions were estimated using the target/decoy method [46]. There were 48,311
914 peptide spectrum matches (PSMs) meeting the FDR cutoff in the male plex. The filtered
915 PSMs were assembled into protein lists using basic and extended parsimony principles
916 and required two distinct peptides per protein. There were 2,805 protein groups in the
917 male plex (excluding common contaminants). The final list of identified proteins, protein
918 groups, and protein families were used to define unique and shared peptides for
919 quantitative use. Total (summed) reporter ion intensities were computed from the PSMs
920 associated with all unique peptides for each protein.

921 The quantitative data for each plex was put on a common intensity scale using the
922 internal reference scaling method described in Plubell et al. 2017 [40]. The intensities of

923 the duplicate pooled standard channels in each plex were used to compute scaling factors
924 to correct for the pseudo-random MS2/MS3 scan selection process and make the pooled
925 standard channel averages in each plex identical. Those scaling factors were applied to
926 all channels containing the biological samples in each plex. The number of quantifiable
927 proteins depends on whether individual plexes or both plexes are considered. There were
928 2,721 quantifiable proteins for the male plex, or 2,610 after intensity scaling using IRS.

929 The protein intensity values for each biological sample in each biological condition
930 were compared for differential protein expression using the Bioconductor package edgeR
931 [47] in Jupyter notebooks. Result tables contained typical proteomics summaries,
932 reporter ion intensities, and statistical testing results. Additional annotations from
933 www.UniProt.org were added (<https://github.com/pwilmart/annotations>).

934 The mass spectrometry instrument data files, sample keys, proteomics results
935 files, and statistical testing notebooks have been deposited to the ProteomeXchange
936 Consortium (<http://proteomecentral.proteomexchange.org>) via the PRIDE partner
937 repository [48] with the dataset identifier PXD036222.

938 6. *STRING-DB analyses*

939 Functional enrichment analysis was performed using STRING (string-db.org). The
940 entire data set consisting of the accession numbers and log fold change for the pair of
941 genotypes being compared was pasted into STRING on the “Proteins with values/ranks”
942 page, and organism *Mus musculus* was chosen. The enriched terms were downloaded
943 and sorted by enrichment score (largest to smallest). Because STRING queries multiple
944 databases including Gene Ontology, Reactome, STRING clusters, Wikipathways,
945 Monarch, etc., many categories were redundant. Tables and images in the paper are of

946 top nonredundant terms. Images of the top networks/pathways were created in STRING
947 using the default settings and exported (protein domain terms were excluded).

948 *7. Statistics*

949 GraphPad Prism version 8.3.0 was used for the generation of survival curves and
950 statistical analysis of the ultrasound data and aortic wall morphology data in mice. Normal
951 distributed ultrasound values were analyzed using one-way ANOVA and Dunnett's
952 multiple comparisons test. For values that were not normally distributed, including major
953 break quantification in the aortic root, the Mann-Whitney-U or the Kruskal-Wallis test with
954 post-hoc Dunn test was applied as well as the Wilcoxon signed-rank test. Results are
955 shown as mean \pm standard deviation. All values in mice are absolute measures, not
956 corrected for length or weight. A p-value of < 0.05 was used to define statistical
957 significance (two-sided).

958

959 **ACKNOWLEDGMENTS**

960 The authors wish to thank Anne De Paepe for financial and moral support. We
961 would also like to thank Gerlinde Logghe and Matthias Van Impe for assistance in data
962 collection and *ex vivo* propagation-based phase-contrast synchrotron imaging. Mass
963 spectrometric analysis was performed by the OHSU Proteomics Shared Resource with
964 partial support from NIH core grants P30EY010572, P30CA069533, and S10OD012246.

965 **FUNDING**

966 This work was supported by a Methusalem grant from the Flemish government
967 and the Ghent University (grant number BOF15/ MET-V/011 to Anne De Paepe); a Grant
968 for Medical Research from the Baillet Latour Fund and a Concerted Research Action

969 grant from the Ghent University Special Research Fund (grant number BOF GOA019-21)
970 to Julie De Backer; the National Institutes of Health (grant number P01AR049698 to
971 Francesco Ramirez and Lynn Sakai); and the Shriners Hospitals for Children (to Lynn
972 Sakai and Doug Keene). Marjolijn Renard was supported as a postdoctoral fellow (grant
973 number FWO 12N6115N and 12N6118N), and Julie De Backer is supported as a senior
974 clinical investigator by the Research Foundation - Flanders. The funders had no role in
975 study design, data collection and analysis, decision to publish, or preparation of the
976 manuscript.

977 **CONFLICT OF INTEREST**

978 The authors declare no conflict of interest.

979

980 **REFERENCES**

- 981 [1] De Paepe, A.D., Devereux, R.B., Dietz, H.C., Hennekam, R.C., & Pyeritz, R.E. (1996).
982 Revised diagnostic criteria for the Marfan syndrome. *Am. J. Med. Genet.* 62, 417-426.
- 983 [2] Pyeritz, R.E. (2000). The Marfan syndrome. *Annu. Rev. Med.* 51, 481-510.
- 984 [3] Sakai, L.Y., Keene, D.R., Renard, M., & De Backer, J. (2016). The disease-causing
985 gene for Marfan syndrome and other genetic disorders. *Gene* 591, 279-291.
- 986 [4] Milewicz, D.M., Braverman, A.C., De Backer, J., Morris, S.A., Boileau, C., Maumenee,
987 I.H., Jondeau, G., Evangelista, A., & Pyeritz, R.E. (2021). Marfan syndrome. *Nat. Rev.*
988 *Dis. Primers* 7, 64.
- 989 [5] Dietz, H.C., McIntosh, I., Sakai, L.Y., Corson, G.M., Chalberg, S.C., Pyeritz, R.E., &
990 Francomano, C. (1993). Four novel FBN1 mutations: significance for mutant transcript
991 level and EGF-like domain calcium binding in the pathogenesis of Marfan syndrome.
992 *Genomics* 17, 468-475.
- 993 [6] Isogai, Z., Ono, R.N., Ushiro, S., Keene, D.R., Chen, Y., Mazzieri, R., Charbonneau,
994 N.L., Reinhardt, D.P., Rifkin, D.B., & Sakai, L.Y. (2003). Latent transforming growth factor
995 β -binding protein 1 interacts with fibrillin and is a microfibril-associated protein. *J. Biol.*
996 *Chem.* 278, 2750-2757.
- 997 [7] Neptune, E.R., Frischmeyer, P.A., Arking, D.E., Myers, L., Bunton, T.E., Gayraud, B.,
998 Ramirez, F., Sakai, L.Y., & Dietz, H.C. (2003). Dysregulation of TGF- β activation
999 contributes to pathogenesis in Marfan syndrome. *Nat. Genet.* 33, 407-411.

1000 [8] Ng, C.M., Cheng, A., Myers, L.A., Martinez-Murillo, F., Jie, C., Bedja, D., Gabrielson,
1001 K.L., Hausladen, J.M.W., Mecham, R.P., Judge, D.P., & Dietz, H.C. (2004). TGF- β -
1002 dependent pathogenesis of mitral valve prolapse in a mouse model of Marfan syndrome.
1003 J. Clin. Invest. 114, 1586-1592.

1004 [9] Habashi, J.P., Judge, D.P., Holm, T.M., Cohn, R.D., Loeys, B.L., Cooper, T.K., Myers,
1005 L., Klein, E.C., Liu, G., Calvi, C., Podowski, M., Neptune, E.R., Halushka, M.K., Bedja,
1006 D., Gabrielson, K., Rifkin, D.B., Carta, L., Ramirez, F., Huso, D.L., & Dietz, H.C. (2006).
1007 Losartan, an AT1 antagonist, prevents aortic aneurysm in a mouse model of Marfan
1008 syndrome. Science 312, 117-121.

1009 [10] Cohn, R.D., van Erp, C., Habashi, J.P., Soleimani, A.A., Klein, E.C., Lisi, M.T.,
1010 Gamradt, M., ap Rhys, C.M., Holm, T.M., Loeys, B.L., Ramirez, F., Judge, D.P., Ward,
1011 C.W., & Dietz, H.C. (2007). Angiotensin II type 1 receptor blockade attenuates TGF- β -
1012 induced failure of muscle regeneration in multiple myopathic states. Nat. Med. 13, 204-
1013 210.

1014 [11] Lacro, R.V., Dietz, H.C., Sleeper, L.A., Yetman, A.T., Bradley, T.J., Colan, S.D.,
1015 Pearson, G.D., Selamet Tierney, E.S., Levine, J.C., Atz, A.M., Benson, D.W., Braverman,
1016 A.C., Chen, S., De Backer, J., Gelb, B.D., Grossfeld, P.D., Klein, G.L., Lai, W.W., Liou,
1017 A., Loeys, B.L., Markham, L.W., Olson, A.K., Paridon, S.M., Pemberton, V.L., Pierpont,
1018 M.E., Pyeritz, R.E., Radojewski, E., Roman, M.J., Sharkey, A.M., Stylianou, M.P.,
1019 Wechsler, S.B., Young, L.T., & Mahony, L. (2014). Atenolol versus losartan in children
1020 and young adults with Marfan's syndrome. N. Engl. J. Med. 371, 2061-2071.

1021 [12] Milleron, O., Arnoult, F., Ropers, J., Aegerter, P., Detaint, D., Delorme, G., Attias,
1022 D., Tubach, F., Dupuis-Girod, S., Plauchu, H., Barthelet, M., Sassolas, F., Pangaud, N.,
1023 Naudion, S., Thomas-Chabaneix, J., Dulac, Y., Edouard, T., Wolf, J.E., Faivre, L., Odent,
1024 S., Basquin, A., Habib, G., Collignon, P., Boileau, C. & Jondeau, G. (2015). Marfan
1025 sarten: a randomized, double-blind, placebo-controlled trial. *Eur. Heart J.* 36, 2160-2166.

1026 [13] Franken, R., den Hartog, A.W., Radonic, T., Micha, D., Maugeri, A., van Dijk, F.S.,
1027 Meijers-Heijboer, H.E., Timmermans, J., Scholte, A.J., van den Berg, M.P., Groenink, M.,
1028 Mulder B.J.M., Zwinderman, A.H., de Waard, V. & Pals, G. (2015). Beneficial outcome
1029 of losartan therapy depends on type of FBN1 mutation in Marfan syndrome. *Circ.*
1030 *Cardiovasc. Genet.* 8, 383-388.

1031 [14] Doyle, J.J., Gerber, E.E. & Dietz, H.C. (2012). Matrix-dependent perturbation of
1032 TGF β signaling and disease. *FEBS Lett.* 586, 2003-2015,

1033 [15] Cook, J.R., Clayton, N.P., Carta, L., Galatioto, J., Chiu, E., Smaldone, S., Nelson,
1034 C.A., Cheng, S.H., Wentworth, B.M. & Ramirez, F. (2015). Dimorphic effects of
1035 transforming growth factor- β signaling during aortic aneurysm progression in mice
1036 suggest a combinatorial therapy for Marfan syndrome. *Arterioscler. Thromb. Vasc. Biol.*
1037 35, 911-917.

1038 [16] Li, W., Li, Q., Jiao, Y., Qin, L., Ali, R., Zhou, J., Ferruzzi, J., Kim, R.W., Geirsson, A.,
1039 Dietz, H.C., Offermanns, S., Humphrey, J.D. & Tellides, G. (2014). *Tgfbr2* disruption in
1040 postnatal smooth muscle impairs aortic wall homeostasis. *J. Clin. Invest.* 124, 755-767.

1041 [17] Ono, R.N., Sengle, G., Charbonneau, N.L., Carlberg, V., Bächinger, H.P., Sasaki,
1042 T., Lee-Arteaga, S., Zilberberg, L., Rifkin, D.B., Ramirez, F., Chu, M-L. & Sakai, L.Y.

1043 (2009). Latent transforming growth factor beta-binding proteins and fibulins compete for
1044 fibrillin-1 and exhibit exquisite specificities in binding sites. *J. Biol. Chem.* 284, 16872-
1045 16881.

1046 [18] Charbonneau, N.L., Carlson, E.J., Tufa, S., Sengle, G., Manalo, E.C., Carlberg,
1047 V.M., Ramirez, F., Keene, D.R. & Sakai, L.Y. (2010). In vivo studies of mutant fibrillin-1
1048 microfibrils. *J. Biol. Chem.* 285, 24943-24955,

1049 [19] Sanford, L.P., Ormsby, I., Gittenberger-de Groot, A.C., Sariola, H., Friedman, R.,
1050 Boivin, G.P., Cardell, E.L. & Doetschman, T. (1997). TGFbeta2 knockout mice have
1051 multiple developmental defects that are non-overlapping with other TGFbeta knockout
1052 phenotypes. *Development* 124, 2659-2670.

1053 [20] Renard, M., Muiño-Mosquera, L., Manalo, E.C., Tufa, S., Carlson, E.J., Keene, D.R.,
1054 De Backer, J. & Sakai, L.Y. (2017). Sex, pregnancy and aortic disease in Marfan
1055 syndrome. *PLoS One* 12, e0181166.

1056 [21] Lindsay, M.E., Schepers, D., Bolar, N.A., Doyle, J.J., Gallo, E., Fert-Bober, J.,
1057 Kempers, M.J.E., Fishman, E.K., Chen, Y., Myers, L., Bjeda, D., Oswald, G., Elias, A.F.,
1058 Levy, H.P., Anderlid, B-M., Yang, M.H., Bongers, E.M.H.F., Timmermans, J., Braverman,
1059 A.C., Canham, N., Mortier, G.R., Brunner, H.G., Byers, P.H., Van Eyk, J., Van Laer, L.,
1060 Dietz, H.C. & Loeys, B.L. (2012). Loss-of-function mutations in TGFB2 cause a
1061 syndromic presentation of thoracic aortic aneurysm. *Nat. Genet.* 44, 922-927.

1062 [22] Charbonneau, N.L., Manalo, E.C., Tufa, S.F., Carlson, E.J., Carlberg, V.M., Keene,
1063 D.R. & Sakai, L.Y. (2020). Fibrillin-1 in the vasculature: in vivo accumulation of eGFP-
1064 tagged fibrillin-1 in a knockin mouse model. *Anat. Rec.* 303:1590-1603.

1065 [23] Verrecchia, F., Chu, M-L. & Mauviel, A. (2001). Identification of novel TGF-
1066 beta/Smad gene targets in dermal fibroblasts using a combined cDNA
1067 microarray/promoter transactivation approach. *J, Biol. Chem.* 276, 17058-17062.

1068 [24] Tellides, G. (2017). Further evidence supporting a protective role of transforming
1069 growth factor- β (TGF β) in aortic aneurysm and dissection. *Arterioscler. Thromb. Vasc.*
1070 *Biol.* 37, 1983-1986.

1071 [25] Sachan, N., Phoon, C. K. L., Zilberberg, L., Kugler, M. C., Ene, T., Mintz, S. B.,
1072 Murtada, S. I., Weiss, D., Fishman, G. I., Humphrey, J. D., & Rifkin, D. B. (2023). TGF β -
1073 2 Haploinsufficiency Causes Early Death in Mice with Marfan Syndrome. *Matrix Biol.*, in
1074 press.

1075 [26] Boileau, C., Guo, D-C., Hanna, N., Regalado, E.S., Detaint, D., Gong, L., Varret, M.,
1076 Prakash, S.K., Li, A.H., D'Indy, H., Braverman, A.C., Grandchamp, B., Kwartler, C.S.,
1077 Gouya, L., Santos-Cortez, R.L.P., Abifadel, M., Leal, S.M., Muti, C., Shendure, J., Gross,
1078 M-S., Rieder, M.J., Vahanian, A., Nickerson, D.A., Michel, J.B., Jondeau, G. & Milewicz,
1079 D.M. (2012). TGFB2 mutations cause familial thoracic aortic aneurysms and dissections
1080 associated with mild systemic features of Marfan syndrome. *Nat. Genet.* 44, 916-921.

1081 [27] Renard, M., Callewaert, B., Malfait, F., Campens, L., Sharif, S., del Campo, M.,
1082 Valenzuela, I., McWilliam, C., Coucke, P., De Paepe, A. & De Backer, J. (2013). Thoracic
1083 aortic-aneurysm and dissection in association with significant mitral valve disease caused
1084 by mutations in TGFB2. *Int. J. Cardiol.* 165, 584-587.

1085 [28] Zilberberg, L., Todorovic, V., Dabovic, B., Horiguchi, M., Couroussé, T., Sakai, L.Y.
1086 & Rifkin, D.B. (2012) Specificity of latent TGF- β binding protein (LTBP) incorporation
1087 into matrix: role of fibrillins and fibronectin. *J. Cell Physiol.* 227, 3828-3836.

1088 [29] Sun, J., Zhang, J., Lindholt, J.S., Sukhova, G.K., Liu, J., He, A., Abrink, M., Pejler,
1089 G., Stevens, R.L., Thompson, R.W., Ennis, T.L., Gurish, M.F., Libby, P. & Shi, G-P.
1090 (2009). Critical role of mast cell chymase in mouse abdominal aortic aneurysm formation.
1091 *Circulation* 120, 973-982.

1092 [30] Zhang, J., Sun, J., Lindholt, J.S., Sukhova, G.K., Sinnamon, M., Stevens, R.L.,
1093 Adachi, R., Libby, P., Thompson, R.W. & Shi, G-P. (2011). Mast cell tryptase deficiency
1094 attenuates mouse abdominal aortic aneurysm. *Circ. Res.* 108, 1316-1327.

1095 [31] Haque, T.T. & Frischmeyer-Guerrero, P.A. (2022). The role of TGF β and other
1096 cytokines in regulating mast cell functions in allergic inflammation. *Int. J. Mol. Sci.* 23,
1097 10864.

1098 [32] Marshall, L.M., Carlson, E.J., O'Malley, J., Snyder, C.K., Charbonneau, N.L.,
1099 Hayflick, S.J., Coselli, J.S., Lemaire, S.A. & Sakai, L.Y. (2013). Thoracic aortic aneurysm
1100 frequency and dissection are associated with fibrillin-1 fragment concentrations in
1101 circulation. *Circ. Res.* 113, 1159-1168.

1102 [33] Carlson, E.J., Rushkin, M., Darby, D., Chau, T., Shirley, R.L., King, J.S., Nguyen,
1103 K., Landry, G.J., Moneta, G.L., Abraham, C., Sakai, L.Y. & Azarbal, A. (2022). Circulating
1104 fibrillin fragment concentrations in patients with and without aortic pathology. *JVS Vas.*
1105 *Sci.*, 3, 389-402.

1106 [34] Sporn, M.B. (2006). The early history of TGF-beta, and a brief glimpse of its future.
1107 Cytokine Growth Factor Rev. 17, 3-7.

1108 [35] Sengle, G. & Sakai, L.Y. (2015). The fibrillin microfibril scaffold: a niche for growth
1109 factors and mechanosensation? Matrix Biol. 47, 3-12.

1110 [36] Bertoli-Avella, A.M., Gillis, E., Morisaki, H., Verhagen, J.M.A, de Graaf, B.M., van de
1111 Beek, G., Gallo, E., Kruithof, B.P.T, Venselaar, H., Myers, L.A., Laga, S., Doyle, A.J.,
1112 Oswald, G., van Cappellen, G.W.A, Yamanaka, I., van der Helm, R.M., Beverloo, B., de
1113 Klein, A., Pardo, L., Lammens, M., Evers, C., Devriendt, K., Dumoulein, M., Timmermans,
1114 J., Bruggenwirth, H.T., Verheijen, F., Rodrigus, I., Baynam, G., Kempers, M., Saenen, J.,
1115 Van Craenenbroeck, E.M., Minatoya, K., Matsukawa, R., Tsukube, T., Kubo, N., Hofstra,
1116 R., Goumans, M.J., Bekkers, J.A., Roos-Hesselink, J.W., van de Laar, I.M.B.H., Dietz,
1117 H.C., Van Lae, r L., Morisaki, T., Wessels, M.W. & Loeys, B.L. (2015). Mutations in a
1118 TGF- β ligand, TGFB3, cause syndromic aortic aneurysms and dissections. J. Am. Coll.
1119 Cardiol. 65, 1324-1336.

1120 [37] Van Reempts, J. & Borgers, M. (1975). A simple polychrome stain for conventionally
1121 fixed epon-embedded tissues. Stain Technol. 50, 19-23.

1122 [38] Logghe, G., Trachet, B., Aslanidou, L., Villaneuva-Perez, P., De Backer, J.,
1123 Stergiopoulos, N., Stampanoni, M., Aoki, H. & Segers, P. (2018). Propagation-based
1124 phase-contrast synchrotron imaging of aortic dissection in mice: from individual elastic
1125 lamella to 3D analysis. Sci. Rep. 8, 2223.

1126 [39] Paganin, D., Mayo, S.C., Gureyev, T.E., Miller, P.R. & Wilkins, S.W. (2002).
1127 Simultaneous phase and amplitude extraction from a single defocused image of a
1128 homogeneous object. J. Microsc. 206, 33-40.

1129 [40] Plubell, D.L., Wilmarth, P.A., Zhao, Y., Fenton, A.M., Minnier, J., Reddy, A.P.,
1130 Klimek, J., Yang, X., David, L.L. & Pamir, N. (2017). Extended multiplexing of tandem
1131 mass tags (TMT) labeling reveals age and high fat diet specific proteome changes in
1132 mouse epididymal adipose tissue. *Mol. Cell. Proteomics* 16, 873-890.

1133 [41] Wilmarth, P.A., Riviere, M.A. & David, L.L. (2009). Techniques for accurate protein
1134 identification in shotgun proteomic studies of human, mouse, bovine, and chicken lenses.
1135 *J. Ocul. Biol. Dis. Infor.* 2, 223-234.

1136 [42] Chambers, M.C., Maclean, B., Burke, R., Amodei, D., Ruderman, D.L., Neumann,
1137 S., Gatto, L., Fischer, B., Pratt, B., Egertson, J., Hoff, K., Kessner, D., Tasman, N.,
1138 Shulman, N., Frewen, B., Baker, T.A., Brusniak, M-Y., Paulse, C., Creasy, D., Flashner,
1139 L., Kani, K., Moulding, C., Seymour, S.L., Nuwaysir, L.M., Lefebvre, B., Kuhlmann, F.,
1140 Roark, J., Rainer, P., Detlev, S., Hemenway, T., Huhmer, A., Langridge, J., Connolly, B.,
1141 Chadick, T., Holly, K., Eckels, J., Deutsch, E.W., Moritz, R.L., Katz, J.E., Agus, D.B.,
1142 MacCoss, M., Tabb, D.L. & Mallick, P. (2012). A cross-platform toolkit for mass
1143 spectrometry and proteomics. *Nat. Biotechnol.* 30, 918-920.

1144 [43] McDonald, W.H., Tabb, D.L., Sadygov, R.G., MacCoss, M.J., Venable, J.,
1145 Graumann, J., Johnson, J.R., Cociorva, D. & Yates III, J.R. (2004). MS1, MS2, and
1146 SQT—three unified, compact, and easily parsed file formats for the storage of shotgun
1147 proteomic spectra and identifications. *Rapid Comm. in Mass Spec*, 18, 2162-2168

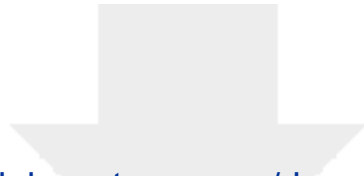
1148 [44] Eng, J.K., Jahan, T.A. & Hoopmann, M.R. (2013). Comet: An open-source MS/MS
1149 sequence database search tool. *Proteomics* 13, 22-24.

1150 [45] Keller, A., Nesvizhskii, A.I., Kolker, E. & Aebersold, R. (2002). Empirical statistical
1151 model to estimate the accuracy of peptide identifications made by MS/MS and database
1152 search. *Anal. Chem.* 74, 5383-5392.

1153 [46] Elias, J.E. & Gygi, S.P. (2007). Target-decoy search strategy for increased
1154 confidence in large-scale protein identifications by mass spectrometry. *Nat. Meth.* 4, 207-
1155 214.

1156 [47] Robinson, M.D., McCarthy, D.J. & Smyth, G.K. (2010). edgeR: a Bioconductor
1157 package for differential expression analysis of digital gene expression data. *Bioinform.*
1158 26, 139-140.

1159 [48] Perez-Riverol, Y., Bai, J., Bandla, C., García-Seisdedos, D., Hewapathirana, S.,
1160 Kamatchinathan, S., Kundu, D.J., Prakash, A., Frericks-Zipper, A., Eisenacher, M.,
1161 Walzer, M., Wang, S., Brazma, A. & Vizcaíno, J.A. (2022). [The PRIDE database](#)
1162 [resources in 2022: a hub for mass spectrometry-based proteomics evidences](#). *Nucleic*
1163 *Acids Res.* 50(D1):D543-D552.



Click here to access/download
e-Component
Supplemental Table 1.xlsx



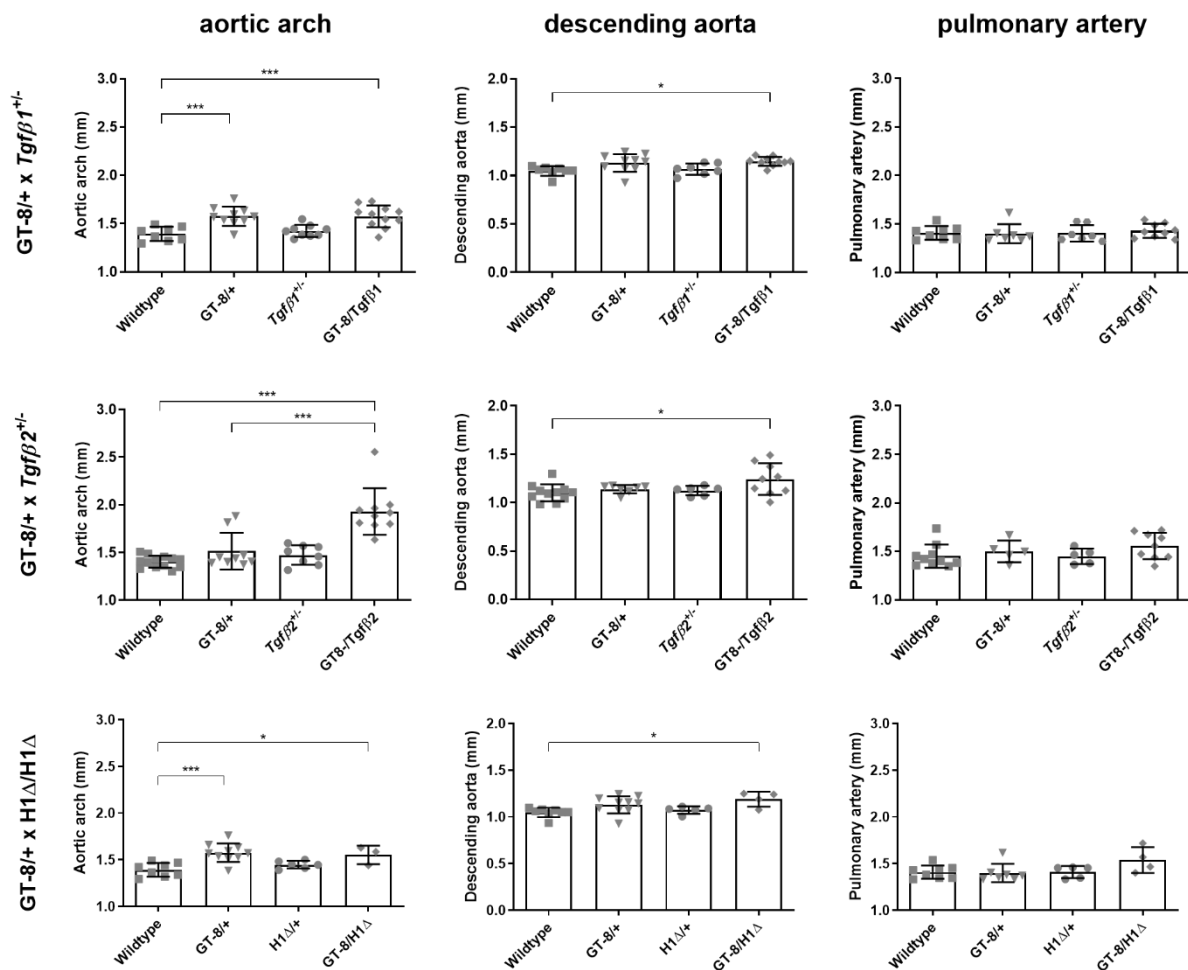
SUPPLEMENTARY MATERIAL

Supplementary Figure 1. Aortic and pulmonary artery dimensions of the studied

mouse models. Cardiovascular ultrasound measurements of the aortic arch, descending aorta, and pulmonary artery dimensions in wildtype and *Fbn1* mutant mice.

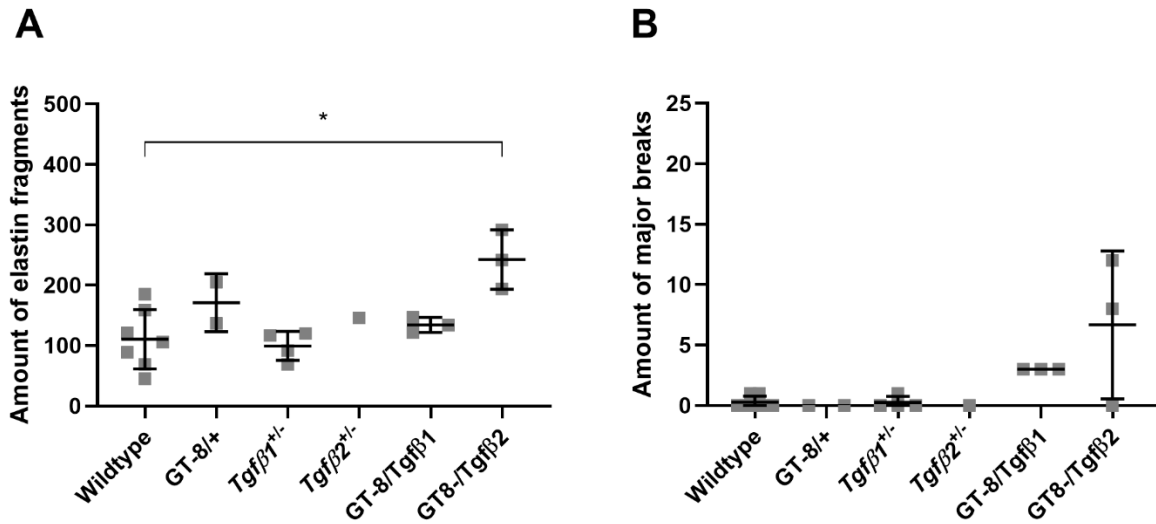
Aortic and pulmonary diameters in 6 month old male mice of the *Tgfb1*^{+/-} cross (top row), *Tgfb2*^{+/-} cross (middle row), and *Fbn1*^{H1Δ/H1Δ} cross (bottom row) are displayed. Results

are presented as mean ± SD. *p < 0.05; **p < 0.01; ***p < 0.001

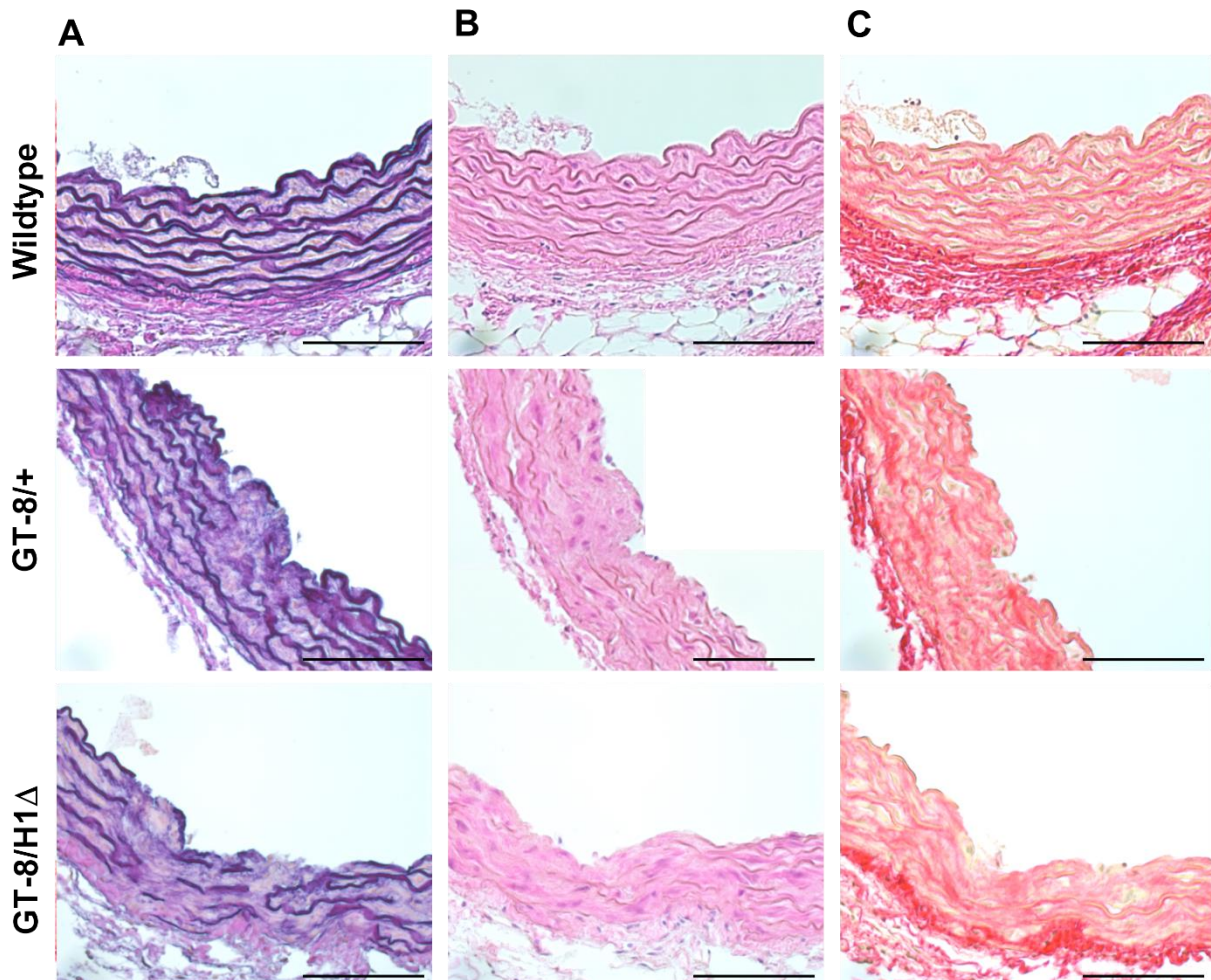


Supplementary Figure 2. Aortic wall morphology in *Fbn1* mutant mouse models.

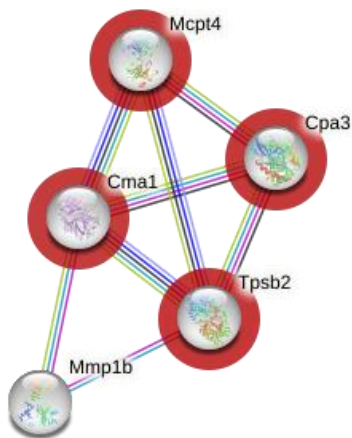
Overview of (A) the number of single breaks in elastic lamellae and (B) the amount of major breaks in the aortic root of 6 month old male wildtype and *Fbn1* mutant mice of the *Tgf β 1*^{+/-} and *Tgf β 2*^{+/-} cross. Results are presented as mean \pm SD. *p < 0.05



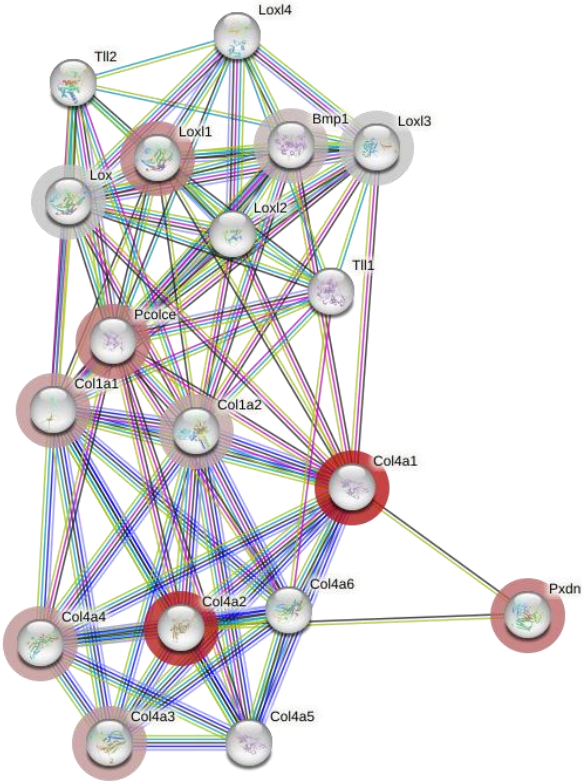
Supplementary Figure 3. Aortic wall morphology in the ascending thoracic aorta of *Fbn1* mutant mice. Histology of the ascending thoracic aorta of a 6 month old male wildtype (top row), GT-8/+ (middle row), and GT-8/H1 Δ mice (bottom row). A) Resorcin-Fuchsin elastin stain. B) H&E staining. C) PSR staining displays. Both GT-8/+ and GT-8/H1 Δ mice display excessive fragmentation of the elastic lamellae and increased collagen deposition in the ascending thoracic aortic wall compared to wildtype. Scale bars = 100 μ m.



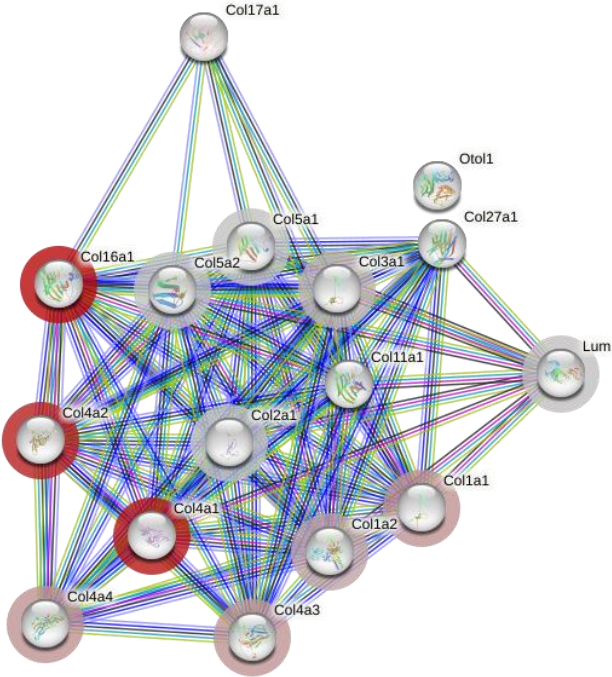
Supplementary Figure 4. Illustrations of STRING-DB enrichment pathways in ascending aorta from Fbn1 mutant mice compared to wildtype. The circles represent a single protein in the network. Haloes indicate that the protein is present in our data set. A blue halo indicates a reduction in the abundance of the protein relative to wildtype, and red haloes show increased abundance. Gray haloes indicate no difference between mutant and wildtype. A) Proteases involved with regulation of angiotensin and basement membrane disassembly were the top enriched pathways in H1Δ mice.



B) In GT-8/+ aorta, enriched networks have increased proteins for (1) crosslinking of collagen, (2) complex of trimers and (3) laminin interactions.

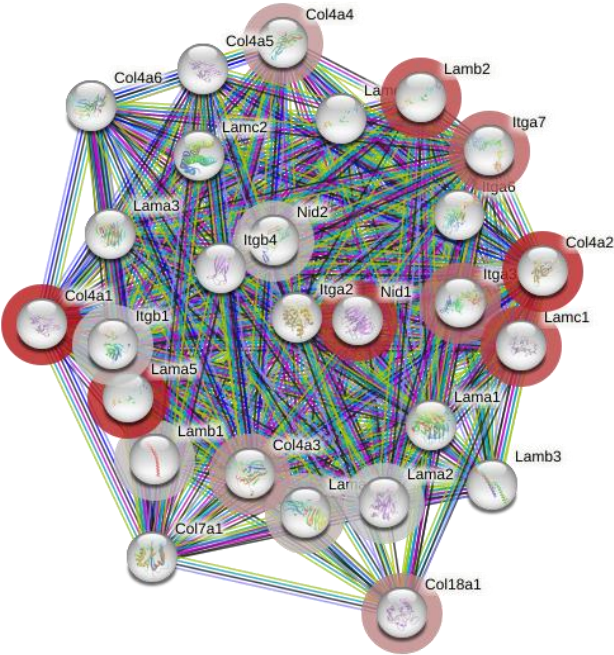


(1)

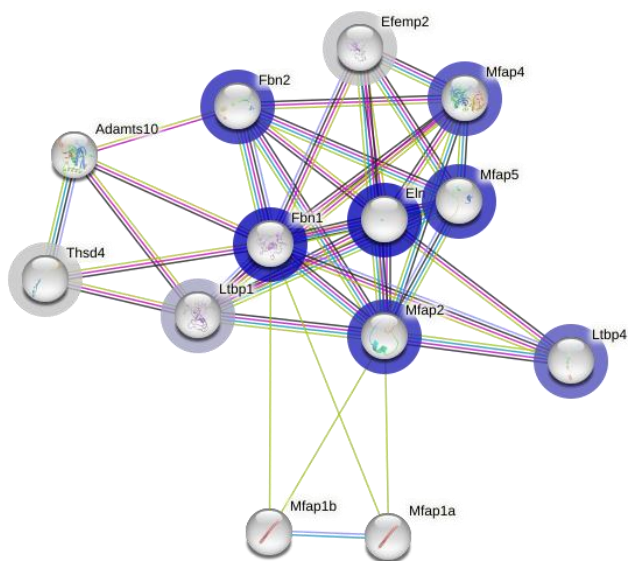


(2)

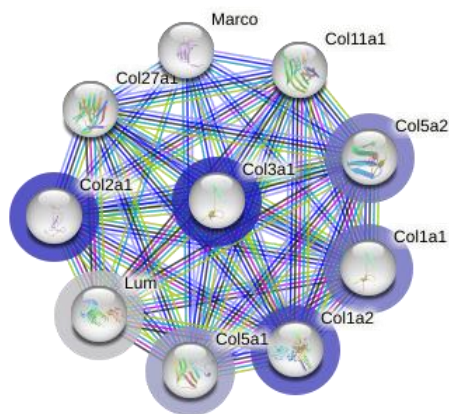
(3)



C) Networks enriched in GT-8/H1Δ are decreased in (1) microfibrils and (2) collagen trimers.



(1)



(2)

Supplementary Table 1A. Orbitrap Fusion Settings for tandem mass spectrometry data collection. Instrument control software version 3.4.3072.18.

General Settings		
	Method duration	140 min
	Ion source type	NSI
	Spray voltage positive ion	2400 V
	Ion transfer tube temperature	305 C
	Internal mass calibration	User defined lock-mass
MS1 Scans		
	Detector	Orbitrap
	MS1 resolution	120,000
	Scan range	400 to 1600 m/z

	Maximum inject time	50 ms
	AGC target	400,000 (100%)
	Microscans	1
	MIPS mode	Peptide
	Minimum intensity	5000
	Charge states	2 to 4
	Include undetermined charge states	FALSE
Dynamic exclusion settings		
	Duration	30 s
	Mass tolerance low	10 ppm
	Mass tolerance high	10 ppm
	Exclude isotopes	TRUE
	Single charge state per precursor	TRUE
MS2 Scans		
	Detector	Linear ion trap
	Quadrupole isolation	2 m/z, no offset
	Fragmentation	CID
	Normalized collision energy	35 %
	Activation	10 ms with Q=0.25
	Scan rate	Rapid
	Maximum inject time	35 ms
	AGC target	10,000
	Scan range	400 to 1600 m/z
	Microscans	1
MS3 scans		
	Detector	Orbitrap
	MS2 isolation window	2
	Number of notches	10
	Fragmentation	HCD
	Normalized collision energy	55 %
	Resolution	50,000
	Scan range	110 to 500
	Maximum inject time	120 ms
	AGC target	125,000 (250%)
	Microscans	1

Supplementary Table 1B. Dionex NCS-3500RS UltiMate Settings: Software

Version: Thermo SII 1.5.0.10747

Buffer Info		
	2D Loading Mobile Phase	10 mM Ammonium Formate, pH 9
	1D Mobile Phase A	0.1% Formic Acid in Water
	1D Mobile Phase B	0.1% Formic Acid in Acetonitrile
2D HPLC		
	2DRPRP Trap Column	Waters NanoEase XBridge BEH130 C18 300 µm x 50 mm column, 5 µm
	Flow Rate	24 µL/min
	Loading Time	10 minutes
1D HPLC		
	Trap Column	Thermo Acclaim PepMap C18 100 µm x 2 cm NanoViper, 5 µm
	Analytical Column	Thermo PepMap RSLC C18, 75 µm x 25 cm EasySpray, 2 µm
	Flow Rate	300 nL/min
	Run Time	140 min
	Starting Mobile Phase	2% Mobile Phase B
1D Gradient Profile		
	<i>Time</i>	<i>Mobile Phase B Composition</i>
	0.0-10.0 min	2%
	10.0-10.1 min	5%
	10.1-110.0 min	25%
	110.0-114.0 min	95%
	114.0-119.0 min	95%
	119.0-120.0 min	2%
	120.0-140.0 min	2%